UNCERTAINTY, AREA, AND VORTICITY CALCULATION ANALYSIS IN AN ANNULAR SECTOR TURBINE CASCADE

MARY GLOVER

Study Project Work, Internal report
Stockholm, Sweden 2013

KTH Industrial Engineering and Management

UNCERTAINTY, AREA, AND VORTICITY CALCULATION ANALYSIS IN AN ANNULAR SECTOR TURBINE CASCADE

Mary Glover

Study Project Work,
2013:??? EKV

Department of Energy Technology
Division of Heat and Power Technology
Royal Institute of Technology
100 44 Stockholm, Sweden

<table>
<tr><td colspan="2">KTH VETENSKAP OCH KONST
KTH Industrial Engineering and Management</td><td>**Study Project Work EGI 2013:??? EKV**

Uncertainty, Area, and Vorticity Calculation Analysis in an Annular Sector Turbine Cascade

Mary Glover</td></tr>
<tr><td>Approved</td><td>Examiner
Prof. Torsten Fransson</td><td>Supervisor
Ranjan Saha</td></tr>
<tr><td></td><td>Commissioner</td><td>Contact person</td></tr>
</table>

ABSTRACT

An analysis of the uncertainties present in measurements from an annular sector turbine cascade was performed. Three different vane configurations were used—one fully cooled case with all cooling holes opened, one uncooled case with all cooling holes blocked, and one partially cooled case with one row of cooling holes opened. Uncertainties in the kinetic energy loss coefficient were found to be highest in the wake region, and near the vane hub and tip for all cooling configurations. Mass-averaged loss uncertainties were found to be higher for the fully cooled case than for the uncooled and partially cooled cases, and partial film cooling was found to reduce the large spike in uncertainty occurring near the tip.

The Matlab script used for post-processing of the data was evaluated for accuracy and limitations, and changes and improvements were made where necessary. Special areas of focus were the area cell calculations, used for mass-averaging the data, and the vorticity calculations. Improvements made to the area calculation method increased the overall accuracy of the results, decreasing the mass-averaged kinetic energy loss coefficient value by up to 1.3%. Axial vorticity calculations revealed a correlation between areas of high vorticity, especially in regions where negative and positive vorticities meet, and high kinetic energy loss coefficient uncertainty.

TABLE OF CONTENTS

LIST OF FIGURES

LIST OF TABLES

NOMENCLATURE

Latin Symbols

A	Area	[m^2]
c	Chord length	[mm]
V	Velocity	[m/s]
s	Pitch	[°]
x	x-coordinate	[mm]
y	y-coordinate	[mm]
z	z-coordinate	[mm]
r	Radius or coordinate in CCS	[mm]
p	Pressure	[Pa]
M	Mach number	[-]
Re	Reynolds number	[-]

Greek Symbols

α	Flow angle	[°]
γ_α	Yaw angle	[°]
β	Pitch angle	[°]
κ	Specific heat ratio	[-]
φ	Coordinate in CCS	[°]
ρ	Density	[kg/m^3]
ζ	Primary loss coefficient	[-]
ω	Vorticity	[1/s]

Subscripts

0	Reference point (stagnation)
1	Upstream of the cascade
2	Downstream of the cascade
ave	Average
ax	Axial reference
c	Stagnation state in absolute frame of reference
hub	Hub
in	Inlet
Iso	Isentropic
le	Leading edge
mid	Midspan
min	Minimum
max	Maximum
out	Outlet
tot	Total
s	Static
te	Trailing edge
tip	Tip

Abbreviations

CAD	Computer Aided Design
CCS	Cylindrical Coordinate System
CD	Converging-Diverging
CFD	Computational Fluid Dynamics
FP	Flow Passage
KTH	Kungl. Tekniska Högskolan
LE	Leading Edge
NGV	Nozzle Guide Vane
PF	Periodicity Factor
PS	Pressure Side
SPF	Simplified Periodicity Factor
SIT	Siemens Industrial Turbomachinery
SS	Suction Side
TE	Trailing Edge
TIT	Turbine Inlet Temperature

1 INTRODUCTION

1.1 Gas Turbine Technology

In recent years as environmental policy has come to the forefront of public and political debate, it has been increasingly recognized that the amount of fossil fuels used in industry must be moderated and cut back. Many have turned to alternative forms of energy production, such as wind and solar energies, but another important branch of research lies in making current energy production methods more efficient.

Figure 1-1 shows the cross-section of a typical gas turbine, as used for power generation. In the compressor stage, cool air is brought to a higher pressure by a set of rotating and stationary blades. This high pressure air is air is mixed with gaseous fuel, and then combusted in the combustion chamber to produce a high temperature gas. This fuel-air mixture passes through the turbine blades, which consists of one row of stationary nozzle guide vanes, and one row of rotating rotor blades, which are designed so as to make the turbine shaft spin. The excess mechanical energy from this rotation is converted to electricity.

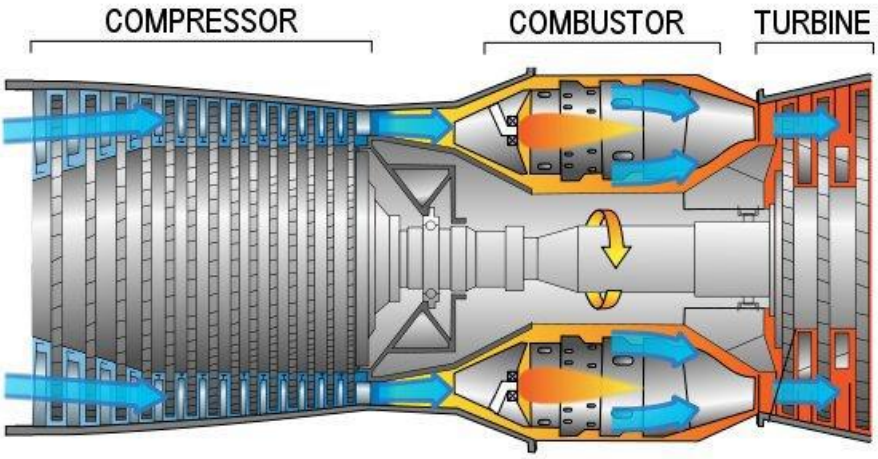

Figure 1-1: Gas turbine cross-section (Bartl 2010, citing Dahl 2007)

Gas turbine technology, commonly used for energy production and aircraft propulsion, is among the most highly developed methods of power generation available today. High turbine efficiencies can be reached by increasing the turbine inlet temperature, with current maximum inlet temperatures reaching between 1800 and 2000K. An upper limit to the positive impact of increased inlet temperature on efficiency has not yet been found. As shown in Figure 1-2, a 55°C increase in inlet temperature leads to a 10% increase in output work and around 1% increase in efficiency.

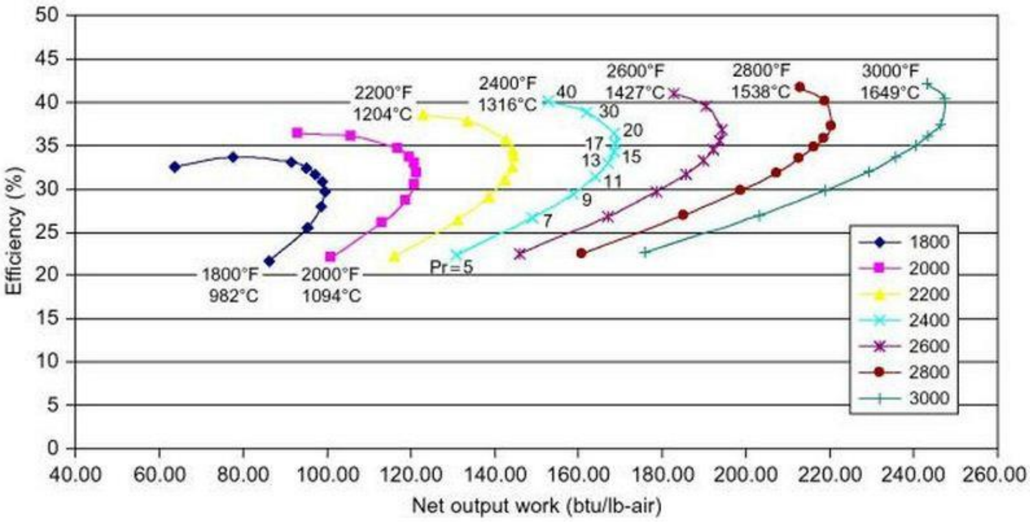

Figure 1-2: Gas turbine performance map (Sudharsan 2012, citing Boyce 2011)

1.2 Secondary Flow Phenomena

The term "secondary flow" is used to describe local flow phenomena that differ from the mainstream flow characteristics. These flow phenomena often occur near to solid boundaries, as a result of the velocity profile in a laminar boundary layer, shown in Figure 1-3. When the flow is subjected to a pressure gradient, the low velocity regions in the boundary layer are affected more, resulting in vortices and other flow phenomena.

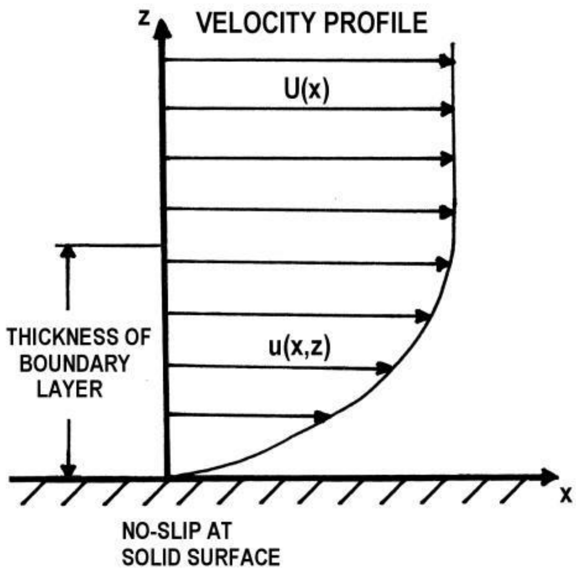

Figure 1-3: Boundary layer velocity profile (Bartl 2010)

Three commonly observed secondary flow phenomena in a turbine cascade are the endwall crossflow, the horseshoe vortex, and the passage vortex. The endwall crossflow occurs when pressure gradients cause a portion of the flow to be deflected from the suction side of one vane to the pressure side of another. The horseshoe vortex forms when the boundary layer hits the leading edge of an NGV. The vortex splits into two legs, one along the PS and one along the SS. The passage vortex results when pressure gradients deflect the PS-leg of the horeshoe vortex toward the SS of the neighboring vane.

Figure 1-4 shows a basic overview of the interaction of secondary flow phenomena, though the reality of secondary flow is much more complex, as the different vortices and crossflows interact with each other. Researchers have developed a number of different secondary flow models containing the three basic secondary flow phenomena, but exact details as to how these phenomena interact with each other are still unknown.

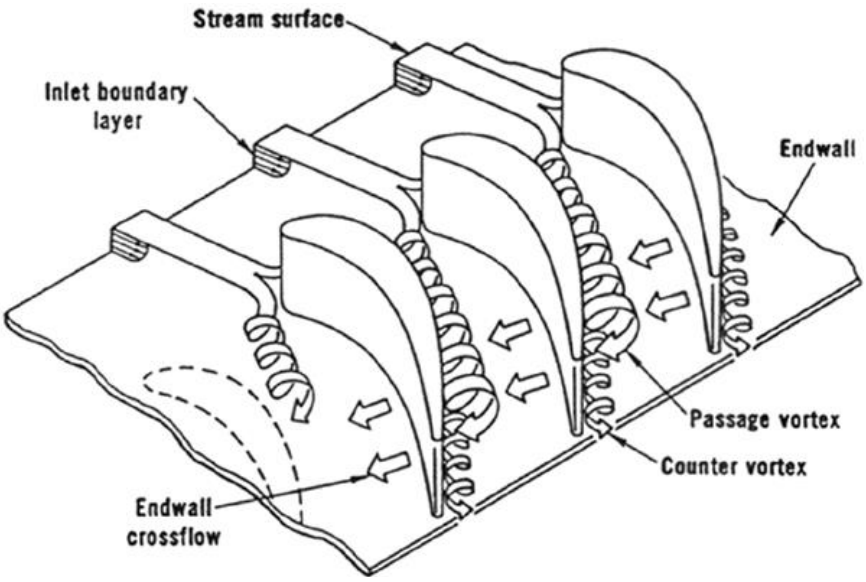

Figure 1-4: Secondary flow phenomena (Langston, Nice, and Hooper 1977)

1.3 Cooling Technology

The inlet temperatures currently used in gas turbines are well above the melting points of the materials used to make the vanes. Cooling techniques, such as film cooling, must be used to protect the NGVs from damage due to these high temperatures. Film cooling is a method through which cool air originating from the compressor is ejected into the turbine cascade through small holes in the NGVs. This cool air forms a protective layer between the vane surface and the hot inlet gas.

The mass flux ratio between the coolant air and the mainstream (also called the blowing ratio), temperature ratio between the coolant air and the mainstream, and the size, geometry, and location of the coolant holes can all impact the film cooling process. The blowing ratio must be optimized for given conditions as a high blowing ratio could lead to the coolant air jet lifting off the vane, thereby reducing the protective effect of the film cooling. The configuration of cooling holes is also important—though vanes subjected to film cooling often experience high aerodynamic losses, the addition of coolant air into the flow can be beneficial in some vane regions (Glodic 2008).

1.4 Previous Studies

Pütz (2010) provided a detailed list of previous studies using the annular sector cascade. These previous studies include:

- Glodic (2008): Investigated the losses for the cooled and uncooled configuration of an annular sector cascade with 50 vanes, rather than the 38 vane cascade used in this study. The rest of the test facility was the same as that used in this study. The study found an increase in losses for the cooled case when compared to the uncooled case, especially in the tip region.

- Gaufrov (2008): Performed numerical simulations to ensure that a new NGV configuration could be installed. The circumferential perioditicy was studied and compared with a periodic case, and the periodicity was found to be unacceptably low, and different outlet configurations were studied as means of improvement. An NGV configuration without a tailboard was determined to have the best perioditicy, though this vane design impacted the radial pressure gradient.
- Schafer (2009): Performed another set of numerical simulations, which added heat shields into the existing models for various operating conditions. A disturbance of the flow was found close to the hub and shroud due to the addition of the heat shields, resulting in higher overall losses and reduced Mach number at the outlet.
- Speer (2009): Designed and tested a new set of vanes. In the study, leakage tests were performed to ensure vane integrity, and the perioditicy of the downstream flow field was checked and found to be acceptable. His study also found an abnormality in the upstream velocity profile, caused by the turbulence grid.
- Bartl (2010): Performed the first experiments with the new vane design. His study was performed with uncooled vanes, and found that the reduced number of vanes (from 50 to 38) did not cause a significant increase in mass-averaged losses. Test runs using oil flow visualization were completed, and an inclination of the stagnation line was found and attributed to the turbulence grid. This finding, coupled with the irregular upstream velocity profile found in the Speer report, made further investigation of the turbulence grid necessary.

The report of Pütz (2010) performed the necessary further investigation of the turbulence grid. This investigation led to switching from the perforated plate turbulence grid used in past studies to a parallel bar grid, which though creating a lower turbulence intensity did not create the problematic irregular upstream velocity profile found when using the perforated plate grid. This report also performed the first investigations of the effect of the new, cooled vanes on secondary flow, and found the cooling to have a strong effect on the development of local vortices. This was found to be especially true in the endwall region, where coolant air contributed to the formation of the horseshoe vortex. Since this report, several other studies on the annular sector cascade have been published.

The report of Sudharsan (2012) compared the kinetic energy loss coefficient distributions, and the mass-averaged kinetic energy loss coefficients, for the uncooled and cooled vane cases. A preliminary uncertainty analysis for the mass-averaged loss coefficient was performed, and the sensitivity of the uncertainty of the mass-averaged loss coefficient to increases in its variables was analyzed.

In Saha et. al. (2012), a new vane design with a leading edge fillet was investigated. No significant changes in overall losses or flow turning was observed, leading to the conclusion that leading edge contouring will not impact the aerodynamic efficiency of NGVs.

El-Gabry et. al. (2012) investigated the interaction between hub film cooling and mainstream flow, for fully cooled and partially cooled (hub coolant holes only) vane. The cooling flow in the hub region was found to have a strong impact on the development of secondary flow phenomena. The report also located a potential local hotspot on the pressure side trailing edge of the vane, where coolant air from the leading edge does not seem to reach.

The report of Saha et. al. (2013) compared the impact of pressure side and suction side film cooling holes on aerodynamic and secondary losses. Suction side cooling holes were found to influence the aerodynamic loss more than pressure side film cooling holes, though aerodynamic loss was strongly impacted by the presence of film cooling for both cases. Secondary losses were found to decrease for all cooling cases when compared to the uncooled case.

2 OBJECTIVES

The first objective of this study is to analyze the post-processing calculations and associated Matlab code used for analyzing the data, focusing on the mass-averaged loss coefficient and the vorticity calculations. Especially important to the analysis of the mass-averaged loss coefficient is the method used to create area cells around each isolated measurement point.

The second objective of this study is to develop a routine for calculating the uncertainty in the kinetic energy loss coefficient, both before and after mass-averaging, and for various cooling configurations. This uncertainty analysis will take into account as many sources of uncertainty in the experimental data as possible.

3 METHOD OF ATTACK

This study made use of a pre-formulated Matlab routine, which was designed to process the data and create plots. Before using the program to produce results, the routine was evaluated for accuracy and possible limitations, and changes were made when necessary. Special areas of focus for the evaluation were calculation of the mass-averaged loss coefficient, specifically the area cells used for mass averaging, and the vorticity. A literature survey was conducted to investigate methods for calculating the vorticity.

In order to carry out the uncertainty analysis, the necessary equations had to be derived and added to the pre-formulated Matlab routine. Once the equations had been formulated and the code was updated, the uncertainty of experimental results was calculated, plotted, and evaluated. This was completed for an uncooled, fully cooled, and paritally cooled vane configuration, and comparisons between the different cooling cases were made.

4 OVERVIEW OF THE TEST FACILITY

4.1 Experimental Setup

4.1.1 The Air Supply System

The pressurized air used in the annular sector cascade is generated by a screw-type compressor. This compressor is driven by a 1 MW electric motor, which can provide the wind tunnel with an air flow of up to 4.7 kg/s at a pressure of 4 bar. Once compressed, the air is at a temperature around 180°C, but is reduced to the 30°C needed for test runs by an air-cooling system. Figure 4-1 shows a schematic of the main-stream air supply system.

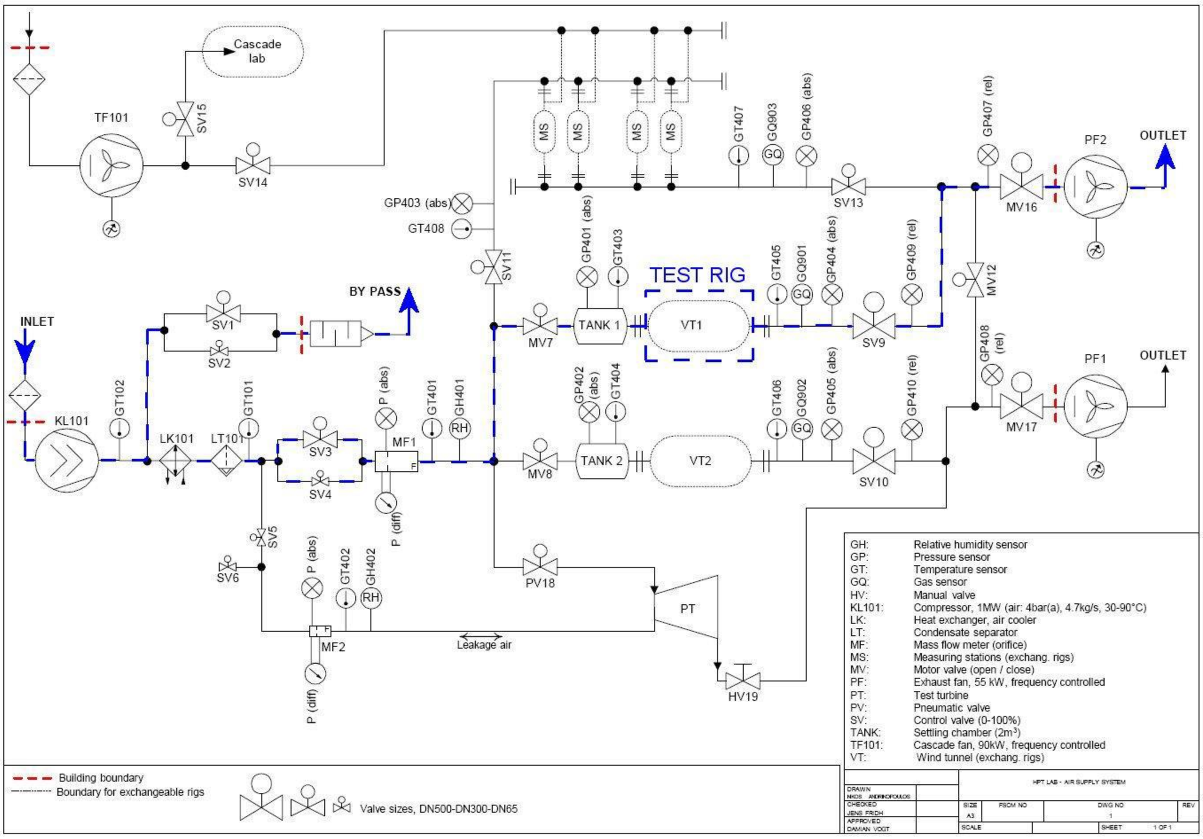

Figure 4-1: The air supply system

The laboratory has two wind tunnels, VT1 and VT2, both of which can be connected to the air supply system by adjusting the valve settings. The blue dashed line in Figure 4-1 shows the flow path during a test run, where the air flow is sent through the annular sector cascade VT1 then continues to the outlet. In this configuration, inlet valves (SV3 and SV4) and by-pass valves (SV1 and SV2) are used to control the inlet mass flow. The outlet valve (SV9) and the exhaust fan (PF2) can be used to adjust the outlet pressure. SV9 is generally kept fully open, and the exhaust fan is used to control outlet pressure. Wind tunnel VT2 is used for calibration measurements.

4.1.2 The Annular Sector Cascade

Figure 4-2 shows the different sections of the wind tunnel. The incoming flow from the compressor (1) is fed to the settling chamber (2), where a honeycomb screen and five mesh screens are used to reduce irregularities in the flow. The flow then passes through a contraction (3), in which the circular shape of the settling chamber is extruded into the annular shape of the test section. Next, the flow passes through a turbulence grid (4), followed by a second radial contraction (5). The flow next passes through the nozzle guide vanes in the test sector (6), and then exits the rig as outflow.

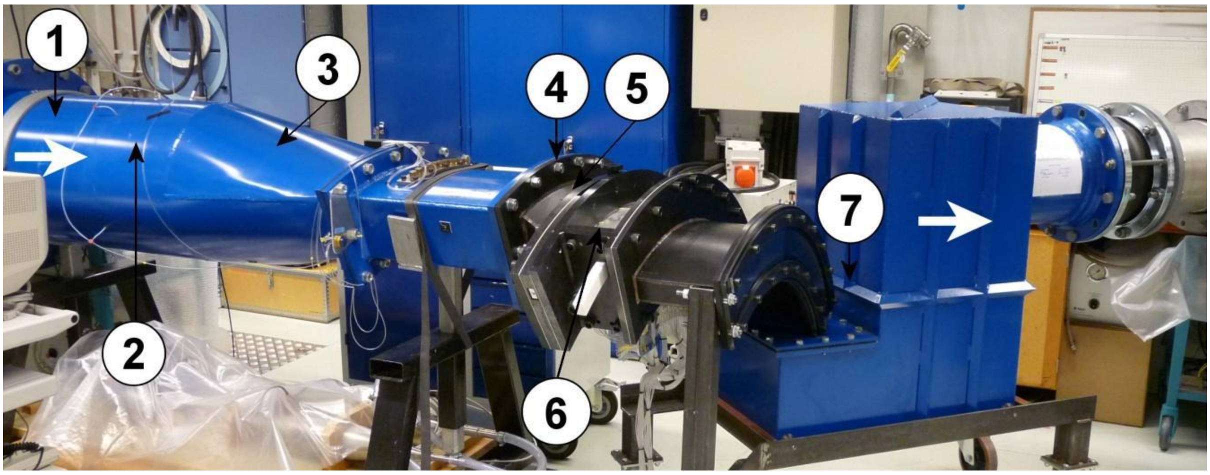

Figure 4-2: Annular sector cascade test rig (Bartl 2010)

Table 4-1: Test rig components, in flow direction

1	Inflow
2	Settling chamber
3	First radial contraction
4	Turbulence grid
5	Second radial contraction
6	Test sector with NGV's
7	Outflow

The turbulence grid used in the annular sector cascade is a parallel bar grid. The flow at the inlet in real turbine applications is highly turbulent, with Tu=10-20% (Roach 1987). There is no inexpensive method to reproduce this high level of turbulence in a laboratory setting, and the turbulence grid used in the test facillity produces turbulence levels of up to 3% (Sudharsan 2012, citing Roux 2004). In Pütz (2010), the influence of the turbulence level on secondary flow and losses was found to be small, making this deviation between the real and experimental flow turbulence conditions acceptable.

4.1.3 The Nozzle Guide Vanes

The annular sector cascade is a 36° annular sector which consists of three nozzle guide vanes and two supporting side walls, which follow the same profile as the vanes. Figure 4-3 shows the NGV cascade. Heat shields are mounted at the hub and tip of the NGV's. The heat shield deflects the inlet boundary layer, which has an impact on the secondary flow phenomena.

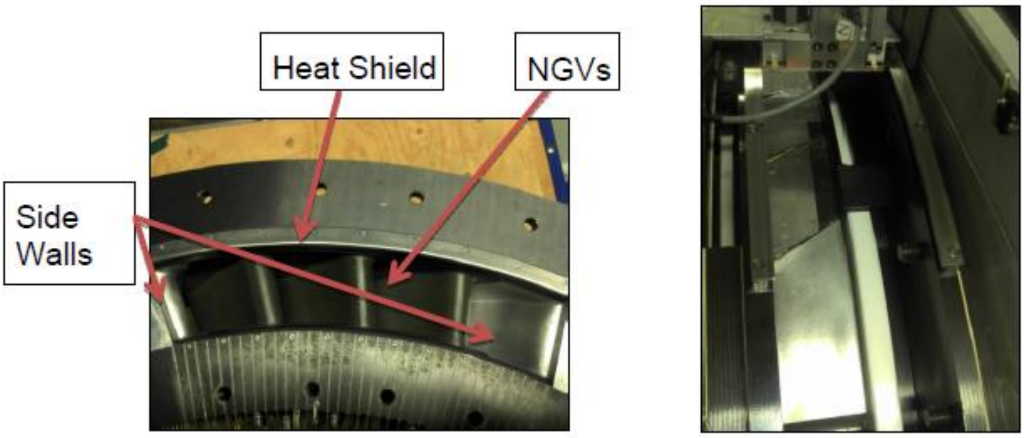

NGV cascade sector (Dismounted) – Downstream to upstream view

NGV cascade sector (Mounted) - As seen from top

Figure 4-3: The NGV cascade (Sudharsan 2012)

The nozzle guide vanes used in this study are equipped with holes to be used for film cooling. Figure 4-4 shows the holes present in the nozzle guide vanes. Holes in rows 1 and 2 are group 1 of the suction side film cooling, while holes in rows 3 and 4 are group 2 of the suction side film cooling. Holes in rows 5 to 10 are used for leading edge film cooling and are referred to as the showerhead cooling holes. Holes in row 11 are used for pressure side film cooling, and holes in row 12 are used for trailing edge cooling.

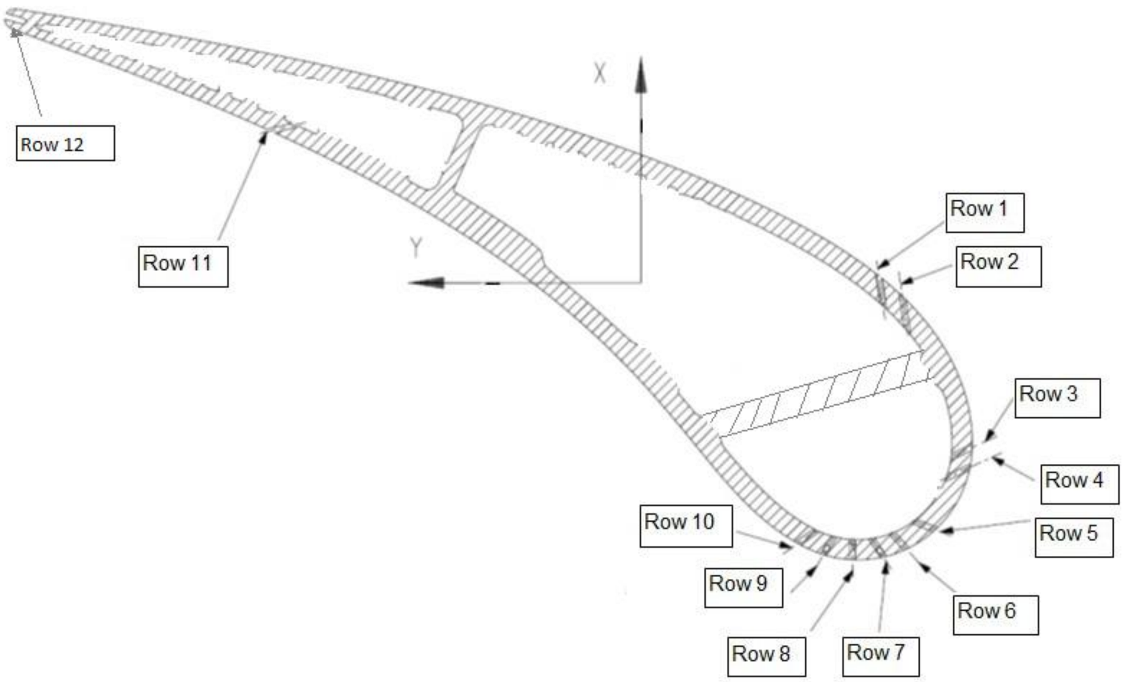

Figure 4-4: Film cooling holes in NGV's (distorted view)

In this report, three measurement sets with different cooling configurations are used. In the uncooled case, all cooing holes are blocked and no coolant air is present in the cascade. In the partially cooled case, only holes in row 7 are open. In the fully cooled case, holes in all rows are open. The cascade design also includes film-cooling holes in the endwall, though these holes are blocked for all trials used in this study.

4.1.4 Setting the Operating Point

The downstream isentropic Mach number is used to confirm repeatability of the experiments and to compare different configurations. This downstream isentropic Mach number is defined as:

$$M_{iso,3} = \sqrt{\frac{2}{k-1}\left[\left(\frac{P_{00}}{P_{avg,3}}\right)^{\frac{k-1}{k}} - 1\right]}$$

In this equation, P_{00} is the total pressure upstream of the guide vanes, and $P_{avg,3}$ is the average value of nine downstream hub static pressure readings at $C_{ax-hub} = 136.5\%$.

4.2 Instrumentation

4.2.1 Pressure Taps

The hub of the test sector contains a total of 139 pressure taps. All are static pressure taps, except PT2131 which is a total pressure tap. As can be seen in Figure 4-5, there are three rows of 35 pressure taps located downstream of the cascade, at 136.5%, 154.9%, and 173.3% C_{ax-hub}, respectively, and one row of 34 pressure taps upstream of the cascade at -30.5% C_{ax-hub}.

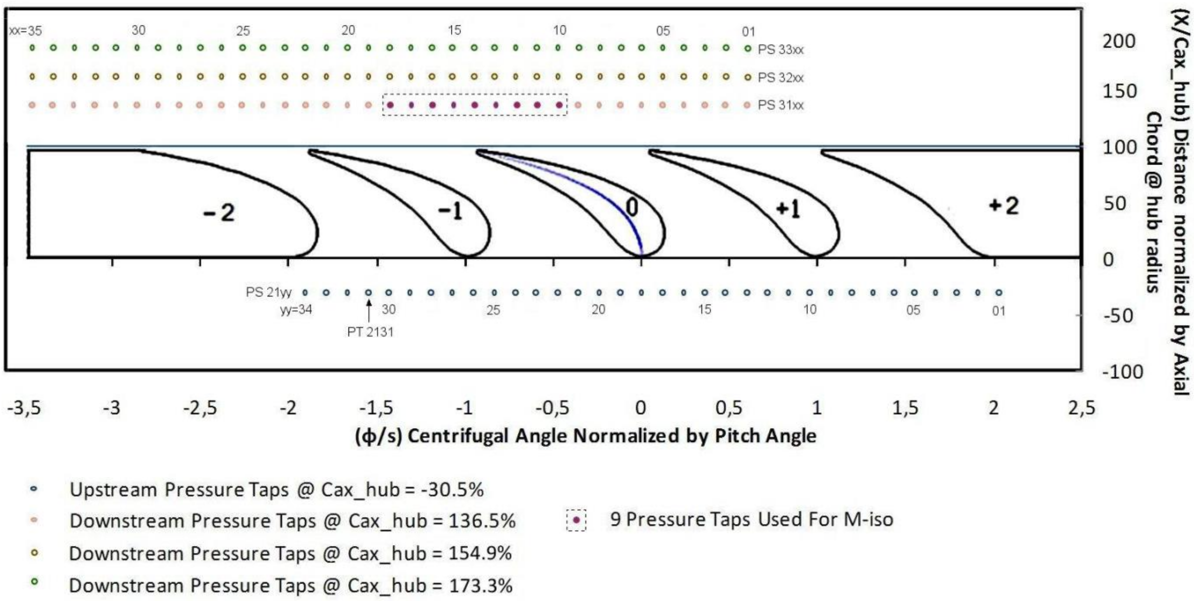

Figure 4-5: Hub pressure taps (Bartl 2010, citing Speer 2009)

The nine pressure taps used for setting the operating point are outlined with a dashed line in Figure 4-5. The pressure taps can also be used to check for periodicity or analyze the downstream flow field within the boundary layer.

4.2.2 Barometer

The atmospheric pressure was measured during the experiment by a Solartron barometer. The barometer has an accuracy of ±0.01% of its full scale, which corresponds to ±11.5 Pa.

4.2.3 Temperature Sensor

The total temperature in the settling chamber is measured using Platinum Resistance Thermometer Pt100. This thermometer has an uncertainty of ±0.15°C at 0°C and an uncertainty of ±0.4°C at 40°C (Pico Technology).

4.2.4 Five-Hole Probe

The flow condition at the outlet is measured using a 5-hole, L-angle probe that is positioned at 127.5% C_{ax-hub}. The geometric features of the five-hole probe used for the experiments can be seen in Figure 4-6. The presence of five holes makes it possible to measure the yaw (flow angle to the radial plane) and pitch (flow angle to the circumferential plane) angles in the flow, along with the total and static pressures. In this way, the five-hole probe is able to capture the entire three-dimensional flow field.

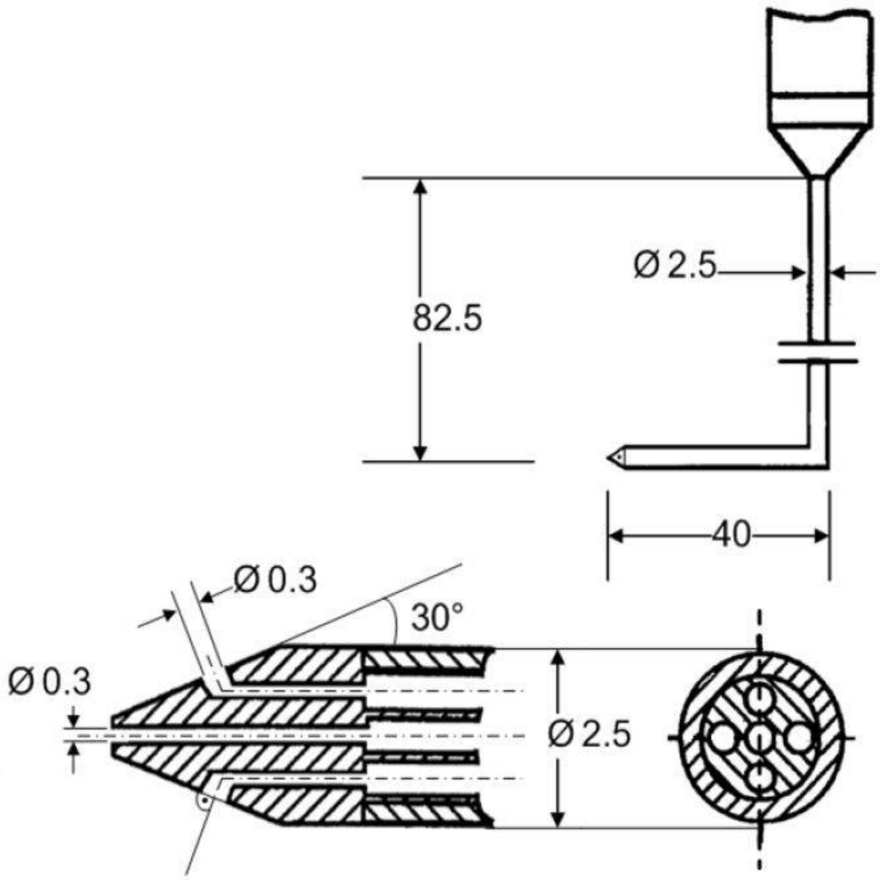

Figure 4-6: The 5-hole probe (Bartl 2010)

4.2.5 Traverse Mechanism

Figure 4-7 shows the two automated traverses that provide radial, circumferential, and yaw motion to the 5-hole probe. The linear traverse unit creates a horizontal motion that is transformed to the circumferential motion of the probe cart by the pin connection and the rails, which guide the cart over the annular cascade. A second traverse unit attached to the cart adjusts the radial and yaw position. The probe is guided in the cascade by a Teflon support sleeve which slides along the sector with the cart. A digital protractor attached to the traverse cart allows the angular position of the cart to be read. The linear traverse unit has a repeatability of ±0.02 mm.

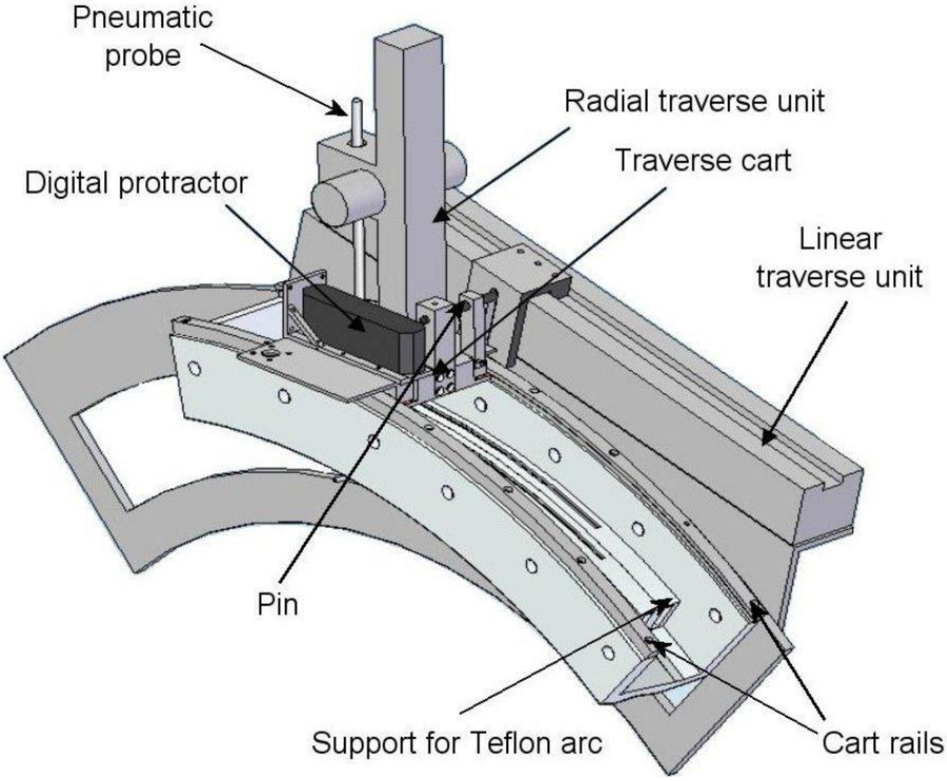

Figure 4-7: The traversing unit (Glodic 2008)

4.2.6 Coolant Mass Flow Controllers

Bronkhrost In-Flow mass flow controllers (MFCs) are used to control the mass flow of the coolant air, which impacts both the coolant air total pressure and the blowing ratio. These can be seen in Figure 4-8. The controllers possess a high accuracy, with a systematic uncertainty of ±0.1% of their full scale, which corresponds to ±0.18 kg/h (Bronkhorst Hi-Tech B.V.).

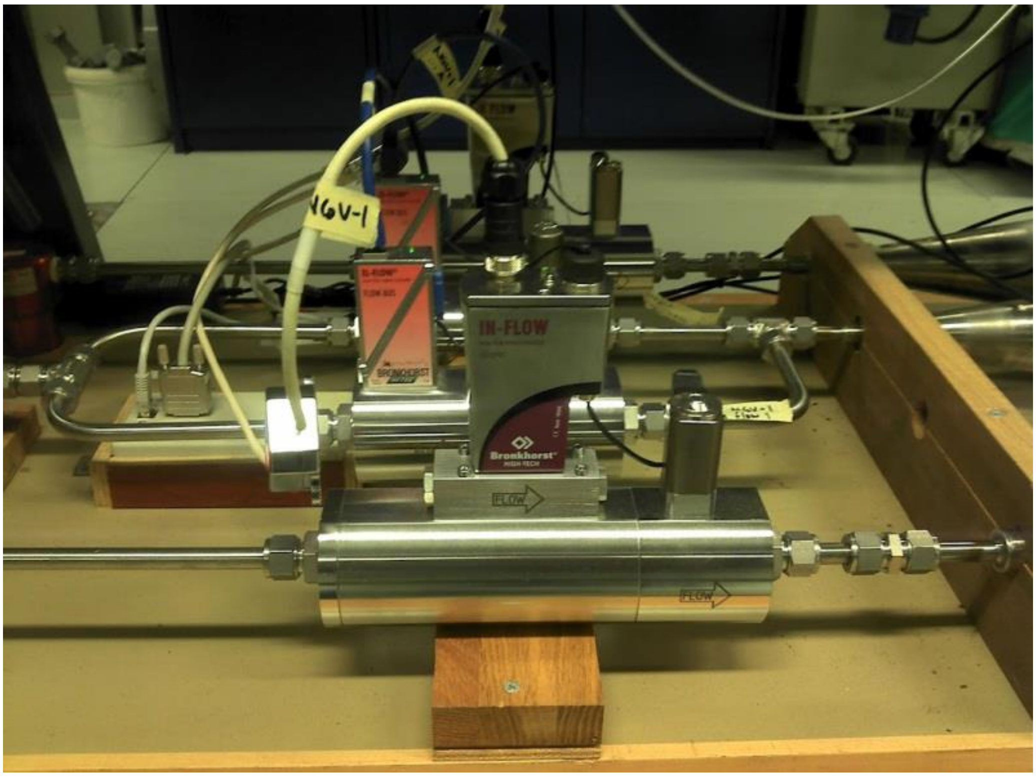

Figure 4-8: Mass flow controller (Sudharsan 2012)

5 DATA PROCESSING

5.1 Matlab Program Architecture

The Matlab function used for post processing the data consists of a main script, eval_trav_MAIN_ASC38_cooled_20130722.m, and a variety of function files that are called for different purposes throughout the script. Figure 5-1 displays an overview of the main routine and the sub-functions it calls.

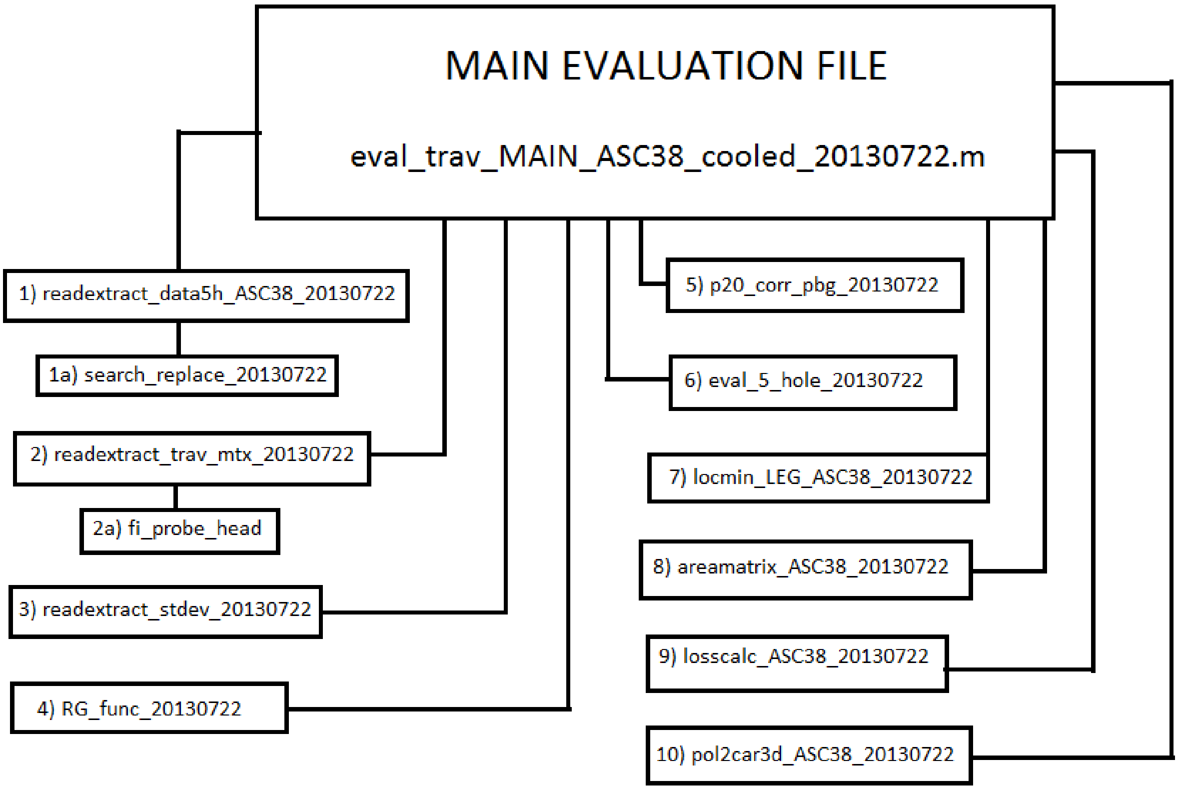

Figure 5-1: Schematic of the Matlab functions used for processing

The main function begins by designating the data set, the associated standard deviation data, and the traverse matrix being used for the calculations. The type of turbulence grid, mass flux ratio *Y*, and pressure loss of the cooling air p_{dp} are also set.

Next, sub-function 1 (readextract_data5h_ASC38_20130722.m) is called. This function sorts the measured data variables into vectors. Function 1a (search_replace_20130722.m) is used to replace all "," in the measured data to ".", to make the format compatible with Matlab when the measurement numbers are used for calculations later in the program.

Sub-function 2 (readextract_trav_mtx_20130722.m) finds the unique radial measurement locations for the traverse cart in the measurement grid, along with the unique positions of the linear traverse cart. Function 2a (fi_probe_head.m) uses geometric relations to obtain the angle "fi", or the circumferential location of the traverse cart, and returns these values to sub-function 2. Geometric relations are used to find the angular and radial locations of the probe head based on the angular and radial locations of the traverse cart.

Sub-function 3 (readextract_stdev_20130722.m) takes the standard deviation data of the measurement points and combines these with the known systematic pressures to find the uncertainties in the raw measurement values used. This process is further explained in Chapter 6.

Sub-function 4 (RG_func_20130722.m) calculates the gas constant and cp-value at each measurement point based on the collected data, and sub-function 5 (p20_corr_pbg_20130722.m) calculates the total pressure at the inlet based on a pre-determined correlation between inlet total pressure and total pressure in the settling chamber. The uncertainty in the value of the gas constant, based on uncertainties in the data values used, is also calculated in sub-function 4.

Returning to the main file, collected data is organized and matrices are prepared for comparison with the 5-hole probe calibration data. Sub-function 6 uses pre-determined calibration coefficients to return the total pressure, static pressure, pitch angle, yaw angle, and Mach number at each measurement point. This is an iterative function, and the routine is repeated until convergence occurs. The uncertainties in the total pressure, static pressure, and Mach number are also calculated in sub-function 6.

Sub-function 7 (loc_min_LEG_ASC38_20130722.m) finds the exact location of the wake by finding the local minimum in downstream total pressure. This location is used as the zero reference point when mass-averaging around one full pitch (i.e. the mass-averaging will range from -0.5*pitch to 0.5*pitch, with the location of the wake set as 0).

Returning to the main file, the data is prepared for mass-averaging, by cutting off those values that lie outside of one pitch around the wake. The static temperature, and its associated uncertainty, are also calculated.

Sub-function 8 (areamatrix_ASC38_20130722.m) calculates the area cell associated with each measurement point, for use in the mass-averaging. The method used to do this is described in detail in Section 5.2. The uncertainty associated with each area cell is also calculated in this function.

Sub-function 9 (losscalc_ASC38_20130722.m) first calculates the true inlet total pressure, using a correlation that differs from that of sub-function 5 (which provides only an estimation). Next, the kinetic energy loss coefficient distribution throughout the measurement grid and a mass-averaged value for each radial measurement point are calculated. The methods used for these loss calculations are described in Section 5.3. The uncertainties in the loss coefficients (both before and after mass-averaging) are calculated in this function. The function also calculates various other mass- and area-averaged values, for use in plotting.

Once the loss coefficients have been calculated, the only task left to the main script is plotting the results. Sub-function 10 (pol2car3d_ASC38_20130722.m) converts the polar coordinates of the probe head into a Cartesian coordinate system, for use in distribution (i.e. non mass-averaged) plots. Various plots are produced by the main script, and these plots can be saved and evaluated as necessary.

5.2 Area Calculations

One of the main results obtained from the measurement data is the mass-averaged kinetic energy loss coefficient, which is calculated over one circumferential pitch at every radial length. In order to calculate this mass-averaged loss coefficient, it is necessary to calculate the area associated with each measurement point used in the calculations.

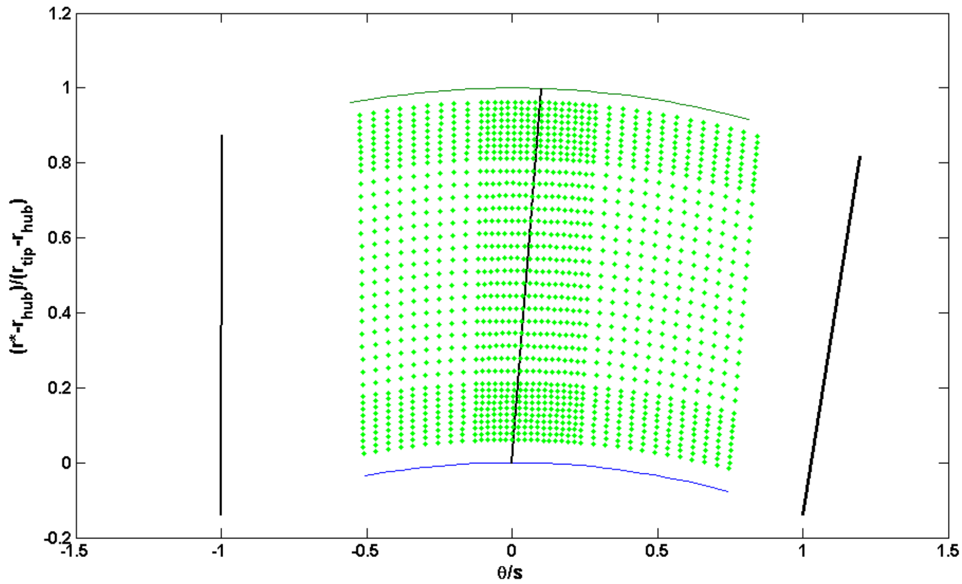

Figure 5-2: Measurement grid used in data collection

Figure 5-2 shows the measurement grid used in data collection. There are 1443 total points, with 37 radial steps and 39 circumferential points in each step. The mass averaging is only performed over one pitch surrounding the trailing edge wake of NGV0, and the start and stop pitchwise locations for this calculation have already been determined in the Matlab sub-function locmin_LEG_ASC38.m.

For data measurement points not on any of the edges of the measurement grid, area calculation is a straightforward process. Each data point is considered as at the center of a small annular sector, as seen in Figure 5-3.

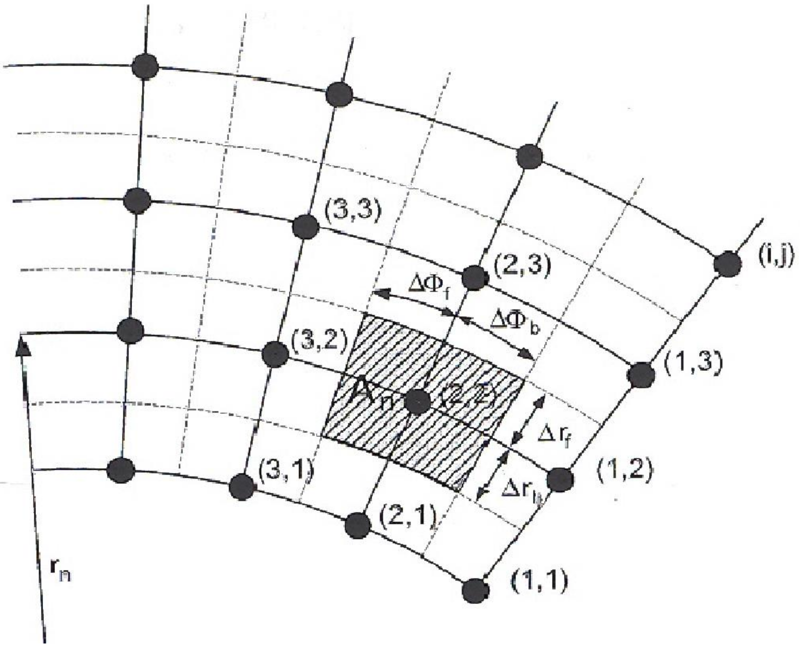

Figure 5-3: Scheme of the area calculations (Glodic 2008, citing Murst 2000)

The area of an annular sector is calculated as $A = \frac{\theta}{2}(R^2 - r^2)$, where *R* is the outer radius of the annulus, *r* is the inner radius, and θ is the span angle of the sector. In the case of these central area cells with radial position r_n and pitchwise position Φ_m, $R = r_n + \Delta r_f$, $r = r_n - \Delta r_b$, and $\theta = \Delta\Phi_f + \Delta\Phi_b$. Here, it is important to note that each Δr value represents one-half the distance between r_n and the radial point either above or below (i.e. $\Delta r_f = \frac{r_{n+1} - r_n}{2}$). Each $\Delta\phi$ value similarly represents one-half the distance between ϕ_m and the circumferential point either to the left or right (so $\Delta\Phi_b = \frac{\Phi_m - \Phi_{m-1}}{2}$ and $\Delta\Phi_f = \frac{\Phi_{m+1} - \Phi_m}{2}$). This makes the overall area calculation for data points not located on any edges of the measurement grid:

$$A_n = \frac{\Phi_{m+1} - \Phi_{m-1}}{4}\left[\left(r_n + \frac{r_{n+1} - r_n}{2}\right)^2 - \left(r_n - \frac{r_n - r_{n-1}}{2}\right)^2\right]$$

For measurement points either on the top or bottom (but not in the corners) of the measurement grid, the data point is still considered to be in the pitchwise center of an annular sector, but its radial position is now either at the top or bottom of the sector. To better visualize the area calculation for top and bottom cells, see measurement point (2,1) in Figure 5-3. This point is at the bottom edge of the measurement grid, so there is no area below the point to be taken into account. When the area around point (2,1) is calculated, the measurement point marks the bottom of the annular sector. The opposite is true for a point at the top edge of the measurement grid—there is no area above the point to be taken into account, so the measurement point marks the top of the annular sector in the area calculations.

For these top and bottom cells with radial position r_n and pitchwise position Φ_m, the area is still calculated as $A_n = \frac{\theta}{2}(R^2 - r^2)$, and the circumferential span is calculated in the same manner as before, but calculation of radii is different. For top cells, $R=r_n$, while r is unchanged. This leads to an area calculation formula of:

$$A_n = \frac{\Phi_{m+1} - \Phi_{m-1}}{4}\left[(r_n)^2 - \left(r_n - \frac{r_n - r_{n-1}}{2}\right)^2\right]$$

For bottom cells, R is unchanged, while $r=r_n$. This leads to an area calculation formula of:

$$A_n = \frac{\Phi_{m+1} - \Phi_{m-1}}{4}\left[\left(r_n + \frac{r_{n+1} - r_n}{2}\right)^2 - (r_n)^2\right]$$

Calculation of area cells on the left and right edge of the pitch (but not in the corners) is more complicated, as steps must be taken to ensure that a full pitch around the NGV0 trailing edge wake is covered. Though the start and stop columns making up one pitch of data are determined in a previous Matlab function file, these values represent the circumferential data points located closest to a span of one pitch, and are not exact. To make up for this, extra area is added to the side cells to ensure that area averaging occurs over a full pitch.

This extra area is added by increasing the angular span of the side cells. θ_{extra} is the pitchwise angle added to each side of the measurement grid and is calculated as $\theta_{extra} = \frac{\frac{360}{38} - (\theta_{stop} - \theta_{start})}{2}$, where θ_{start} is the pitchwise starting point located for area calculations and θ_{stop} is the pitchwise ending point. This calculation first compares the full span of the measurement grid to one pitch ($\frac{360\ degrees}{38\ vanes}$ represents one pitch), and divides this result by two so that an equal amount of area can be added to each side of the grid.

To better visualize the area calculation for left and right cells, see measurement point (1,2) in Figure 5-3. This point is at the right edge of the measurement grid, but extra area must be added to the right of the point to ensure that a full pitch is covered in the area averaging. This is done by making adding θ_{extra} to the span angle of annular sector, meaning $\theta = (\frac{\Phi_{m+1} - \Phi_m}{2})$-($\Phi_m - \theta_{extra}$). For cells on the right side of the grid, θ_{extra} is subtracted from ϕ_m, while for cells on the left side θ_{extra} is added to ϕ_m. The area cells are designed such that the measurement points are in the radial center of the annular sector, so radii are calculated as for the non-edge cells. This makes the area calculation for cells on the left edge of the grid:

$$A_n = \frac{\left(\frac{\Phi_m - \Phi_{m-1}}{2}\right) + \theta_{extra}}{2}\left[\left(r_n + \frac{r_{n+1} - r_n}{2}\right)^2 - \left(r_n - \frac{r_n - r_{n-1}}{2}\right)^2\right]$$

and the area calculation for the cells on the right edge of the grid becomes:

$$A_n = \frac{\left(\frac{\Phi_{m+1} - \Phi_m}{2}\right) + \theta_{extra}}{2}\left[\left(r_n + \frac{r_{n+1} - r_n}{2}\right)^2 - \left(r_n - \frac{r_n - r_{n-1}}{2}\right)^2\right]$$

For measurement points on the corners of the grid, area is calculated as though the measurement point is on the outermost corner of the annular sector. Extra area is again added to ensure the area is calculated over a full pitch, using the same θ_{extra} as above. To better visualize the calculation of corner areas, see measurement point (1,1) in Figure 5-3. There is no area below the corner to be taken into account, and no area to the right of the point to be taken into account except the extra area added through use of θ_{extra}. The area calculation for each the four corners of the measurement grid is as follows:

Top left corner:

$$A_n = \frac{\left(\frac{\Phi_m - \Phi_{m-1}}{2}\right) + \theta_{extra}}{2}\left[(r_n)^2 - \left(r_n - \frac{r_n - r_{n-1}}{2}\right)^2\right]$$

Bottom left corner:

$$A_n = \frac{\left(\frac{\Phi_m - \Phi_{m-1}}{2}\right) + \theta_{extra}}{2}\left[\left(r_n + \frac{r_{n+1} - r_n}{2}\right)^2 - (r_n)^2\right]$$

Top right corner:

$$A_n = \frac{\left(\frac{\Phi_{m+1} - \Phi_m}{2}\right) + \theta_{extra}}{2}\left[(r_n)^2 - \left(r_n - \frac{r_n - r_{n-1}}{2}\right)^2\right]$$

Bottom right corner:

$$A_n = \frac{\left(\frac{\Phi_{m+1} - \Phi_m}{2}\right) + \theta_{extra}}{2}\left[\left(r_n + \frac{r_{n+1} - r_n}{2}\right)^2 - (r_n)^2\right]$$

5.2.1 Comparison to Previous Area Calculation Method

There are three main differences between the old and new area calculation methods. The first difference is the method of determining θ_{extra}. The two different methods for calculating θ_{extra} are below:

$$\text{Old code: } \theta_{extra} = \frac{(\theta_{stop} - \theta_{start}) - \frac{360}{38}}{2}$$

$$\text{New code: } \theta_{extra} = \frac{\frac{360}{38} - (\theta_{stop} - \theta_{start})}{2}$$

The difference between these two equations is merely one of sign convention. In the old code, θ_{extra} was negative where it should have been positive, and vice versa. This meant that when the total span $\theta_{stop} - \theta_{start}$ was less than one full pitch, extra area was subtracted from the edge cells, but should have been added.

The second difference between the old and new calculation methods is the calculation of the span angle for the left and right edge cells. In the angles were calculated by:

$$\text{Left cells: } \frac{\Phi_m - \Phi_{m-1} + \theta_{extra}}{4}$$

$$\text{Right cells: } \frac{\Phi_{m+1} - \Phi_m + \theta_{extra}}{4}$$

This method of calculated the span angle resulted in θ_{extra} being divided by 2 when it was unnecessary. θ_{extra} has already been calculated so that the extra area is split evenly between the two sides of the grid, so no additional changes needed to be made to the angle. This method resulted in a smaller addition to the edge cell area than what was warranted. The new code fixes this issue:

$$\text{Left cells: } \frac{\left(\frac{\Phi_m - \Phi_{m-1}}{2}\right) + \theta_{extra}}{2}$$

$$\text{Right cells: } \frac{\left(\frac{\Phi_{m+1} - \Phi_m}{2}\right) + \theta_{extra}}{2}$$

The third difference between the old and new area calculation methods is that in the new method, θ_{extra} was incorporated into the area calculation for the corner cells, while in the old code it had been not been taken into account.

5.2.2 Impact of New Calculation Method on Results

The method for calculating area of top, bottom, and central cells was not changed. However, the left and right edge cells, along with all four corner cells, experienced an increase in calculated area due to the changes in the method. The corrected θ_{extra} sign convention and modified span angle formula in the new method led to a 30.4% increase in area for all non-corner left and right edge cells. The inclusion of θ_{extra} in the corner cell calculations led to an 18.4% increase in the area of each of these cells. These area increases can be seen graphically in Figure 5-4.

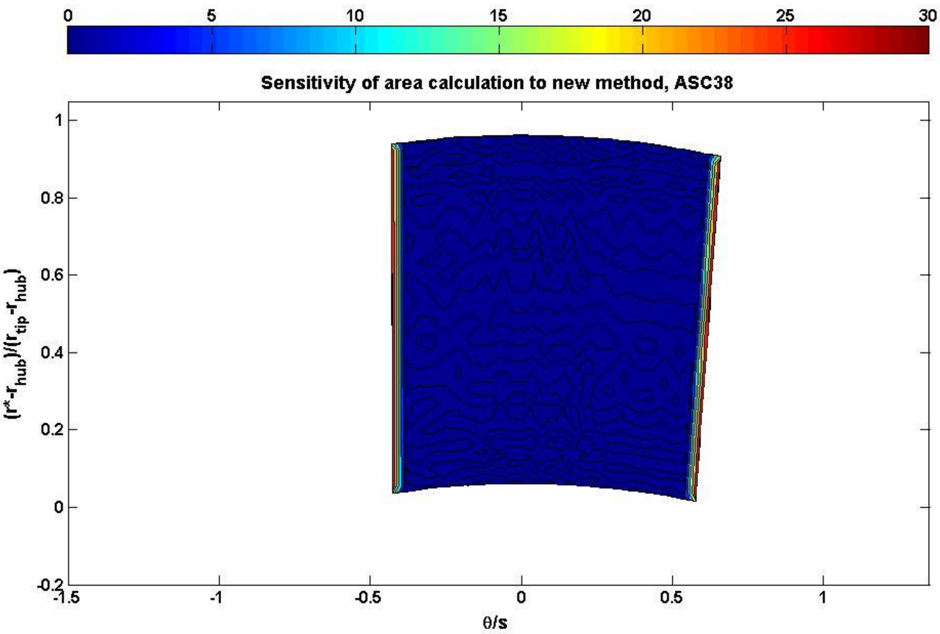

Figure 5-4: Percent change in area due to new method

Though the impact of the new area calculation method on individual edge and corner cells was quite large, the overall impact of the new method on results was smaller. Figure 5-5 shows a sensitivity analysis of various mass- and area-averaged values to the new area calculation method. The new area calculation method causes the largest change in the mass-averaged kinetic energy coefficient and the mass-averaged pressure loss value, with maximum changes of -1.3%. The area-averaged yaw angle changes by a maximum of -0.4%, area averaged static pressure changes by a maximum of -0.1%, and mass-averaged Mach number changes by approximately +0.1%. Mass-averaged total pressure remains almost entirely unchanged.

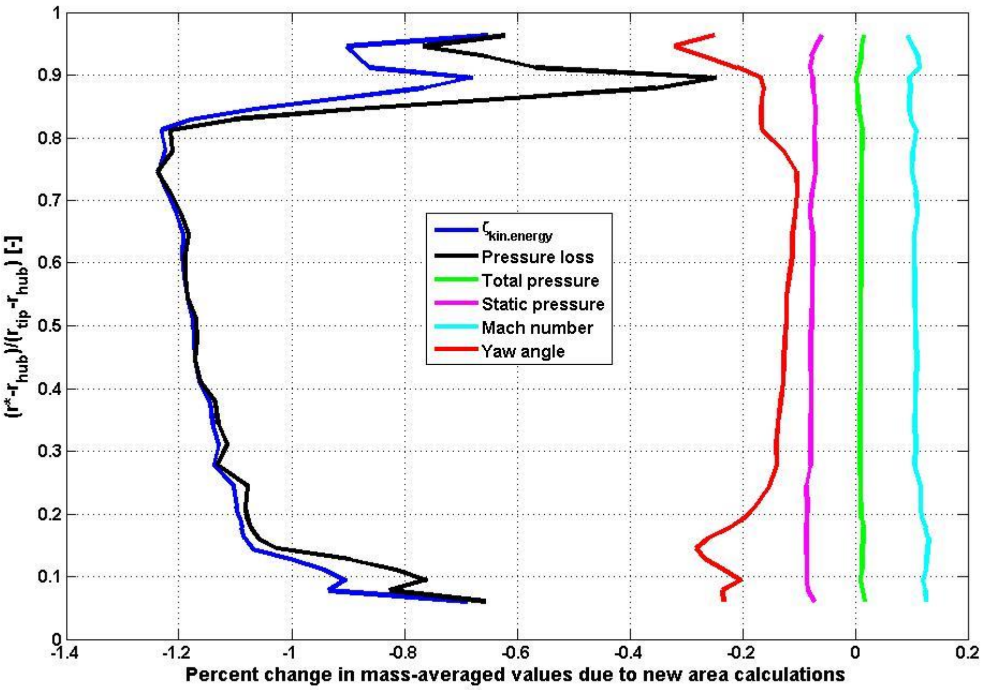

Figure 5-5: Sensitivity to new area calculation method

Though the magnitudes of changes due to the new area calculation method are not large in most cases, the new area calculation method does impact the overall accuracy of the calculated results.

5.3 Loss Calculations

The kinetic energy loss coefficient is among the most important values obtained in the post-processing calculations with Matlab. There are two different formulas for obtaining the kinetic energy loss coefficient, one for the cooled cases (this could include full cooling or various partial cooling setups) and one for the uncooled case. The difference between these two equations arises from the fact that, in the uncooled case, the mass flux ratio Y between the coolant flow and the mainstream flow is 0, as there is no coolant flow present in the uncooled vanes.

The equation used to calculate the kinetic energy loss coefficient for the cooled cases is:

$$\zeta_{kin} = 1 - \frac{(1+Y)\left[1-\left(\frac{p_{30s}}{p_{30}}\right)^{\frac{k-1}{k}}\right]}{1-\left(\frac{p_{30s}}{p_{20}}\right)^{\frac{k-1}{k}} + Y\left[1-\left(\frac{p_{30s}}{p_{cool}-p_{dp}}\right)^{\frac{k-1}{k}}\right]}$$

where p_{30s} is the static pressure measured by the 5-hole probe, p_{30} is the total pressure measured by the 5-hole probe, p_{20} is the total pressure just upstream of the nozzle guide vanes, p_{cool} is the total pressure of the coolant air measured at the plenum chamber, and p_{dp} is the pressure loss in the coolant flow between the plenum chamber and the coolant holes in the vane. Y is the mass flux ratio, and k is the specific heat ratio. Of these values, p_{30s}, p_{30}, p_{20} must be calculated from the collected data values, while p_{cool} is directly measured during the experiments. Y is calculated from the collected mass flow rates, p_{dp} has already been determined before beginning the experiments, and k is assumed to be 1.4.

The equation used to calculate the kinetic energy loss coefficient for the uncooled case is:

$$\zeta_{kin} = \frac{\left(\frac{p_{30s}}{p_{30}}\right)^{\frac{k-1}{k}} - \left(\frac{p_{30s}}{p_{20}}\right)^{\frac{k-1}{k}}}{1-\left(\frac{p_{30s}}{p_{20}}\right)^{\frac{k-1}{k}}}$$

Figures 5-6, 5-7, and 5-8 show the distribution of the kinetic energy loss coefficient across the measurement grid for the cooled, partially cooled, and uncooled case, respectively.

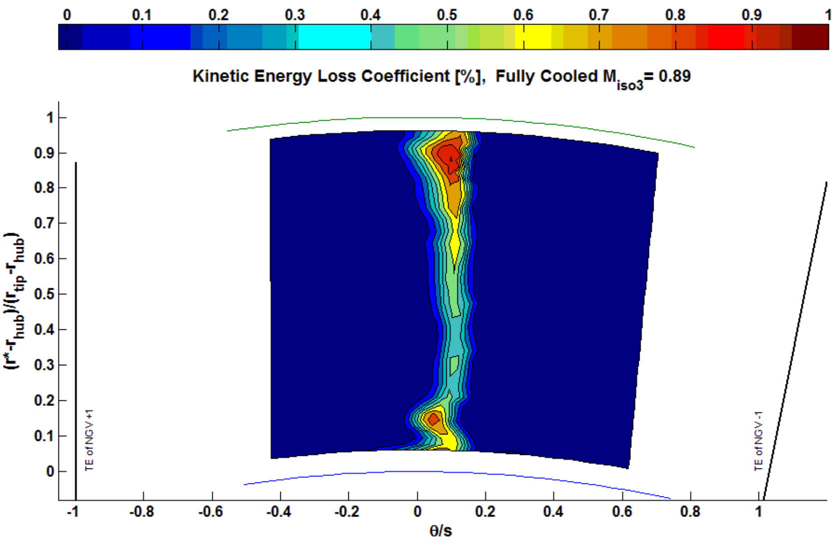

Figure 5-6: Kinetic energy loss coefficient distribution, cooled vane

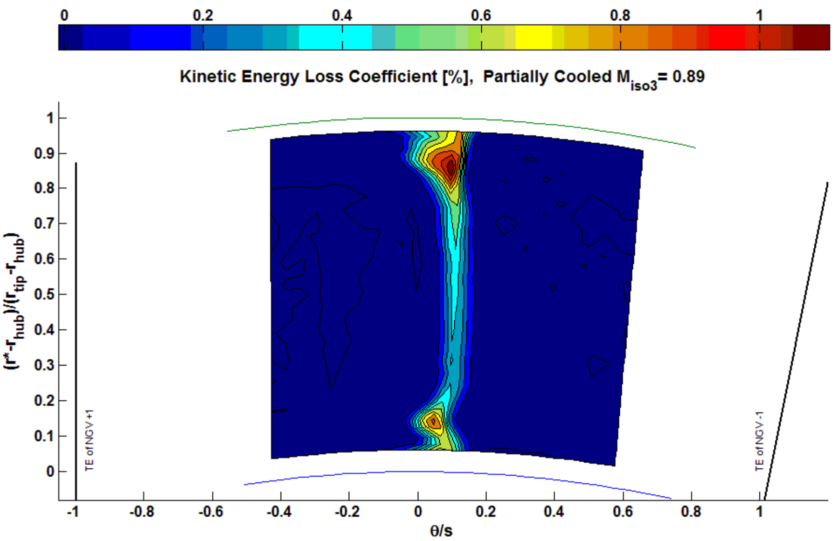

Figure 5-7: Kinetic energy loss coefficient distribution, partially cooled vane

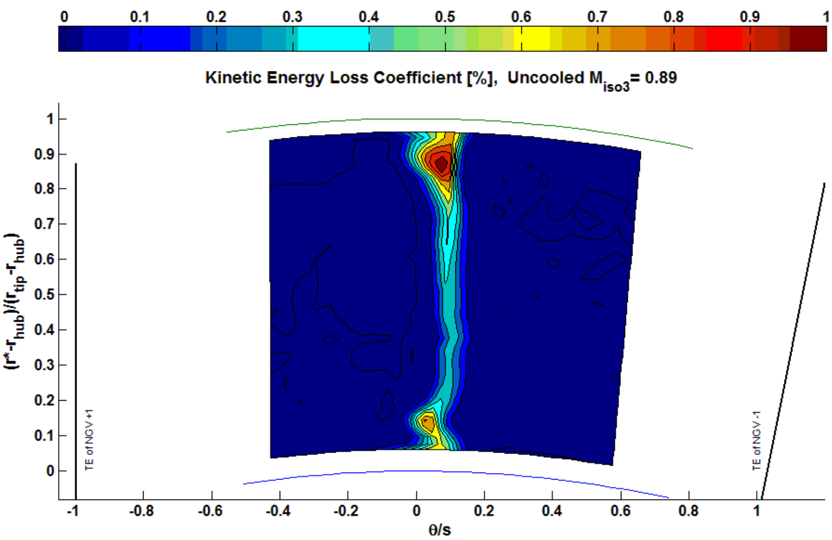

Figure 5-8: Kinetic energy loss coefficient distribution, uncooled vane

General trends in the kinetic energy loss coefficient distribution can be observed. First, the loss coefficient is very low for all cases in most parts of the measurement grid, but is much higher in the wake region. This is especially true near the hub and tip, where concentrated areas with high losses occur. The loss distributions for the uncooled the partially cooled vane configurations are very similar. The distribution for the fully cooled vane configuration is slightly different—losses throughout the wake region are higher, and the concentrated areas with high losses near the hub and tip are larger. This implies that losses for the uncooled and partially cooled configurations are larger, whiles those for the fully cooled case are higher.

The mass-averaged kinetic energy loss coefficient is another important value obtained through the post-processing calculations with Matlab. The mass-averaging is performed at each radial length over one full spanwise pitch. The mass-averaged loss coefficient is calculated as follows:

$$\zeta_{kin,avg} = \frac{\sum_{i=1}^{r} \rho_i A_i c_{ax,i} \zeta_{kin,i}}{\sum_{i=1}^{r} \rho_i A_i c_{ax,i}}$$

5.4 Vorticity Calculations

5.4.1 The Axial Vorticity Component

Mathematically, the vorticity is defined as the curl of the velocity vector, and is calculated as:

$$\omega = \nabla \times \vec{v}$$

The first step towards calculating the axial component of vorticity was to calculate the velocity vectors using the Cartesian coordinate system shown in Figure 5-9.

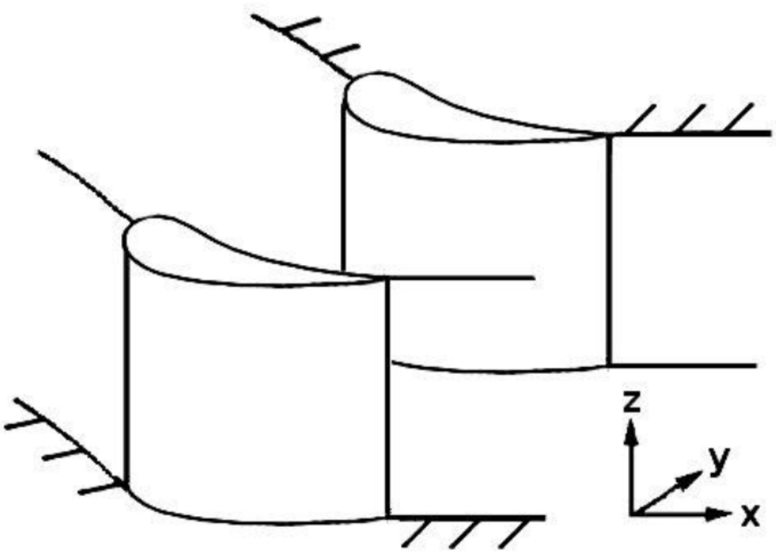

Figure 5-9: Reference coordinate system

In this coordinate system the velocity can be defined by:

$$\vec{v} = \begin{pmatrix} V_x \\ V_y \\ V_z \end{pmatrix}$$

Here, V_y represents the circumferential velocity component and V_z represents the radial velocity component. These two components of the velocity can be calculated by:

$$V_y = Vsin\alpha$$
$$V_z = Vsin\beta$$

where α and β are the yaw and pitch angles, respectively and V is the absolute magnitude of the velocity, calculated by:

$$V = Ma$$

where *M* is the Mach number and *a* is the speed of sound in air.

After calculating the components of the velocity, the axial component of the vorticity can be calculated by:

$$\omega_x = \frac{\partial V_z}{\partial y} - \frac{\partial V_y}{\partial z}$$

Here, it is important to understand the physical meaning of the axial vorticity. A positive vorticity value means that the rate of change of the circumferential velocity component is greater than the rate of change of the radial velocity component. This results in a counterclockwise rotating vortex. A negative vorticity value means that the rate of change of the radial velocity component is greater than the rate of change of the circumferential velocity component. This results in a clockwise rotating vortex.

The differentials for the vorticity calculation are estimated using the gradient function in Matlab, which calculates the value of the differential at each point by:

$$\frac{\partial V_z}{\partial y} \approx \frac{\Delta V_z}{\Delta y}$$

and

$$\frac{\partial V_y}{\partial z} \approx \frac{\Delta V_y}{\Delta z}$$

This method of estimating the value of a differential can be very accurate in a dense measurement field, but it can be seen in Figure 5-1 that measurement points are often not located close together, especially in areas away from the trailing edge, hub, and tip regions. It is worth noting that these regions are subject to few secondary flow effects, and as shown in Figure 5-6 to 5-8 are also areas where overall losses are low. Due to this, it can be expected that conditions in these regions are not changing rapidly, and so the gradient estimation may still be accurate, even without a dense spacing of measurement points. The gradient estimation may also have limited accuracy in the regions with a dense measurement grid, as these regions (near the hub, tip, and trailing edge) are subject to different flow effects and, as a result, rapidly changing conditions.

Figures 5-10, 5-11, and 5-12 display the vorticity distribution throughout the measurement grid for the uncooled, partially cooled, and fully cooled vane configurations, respectively.

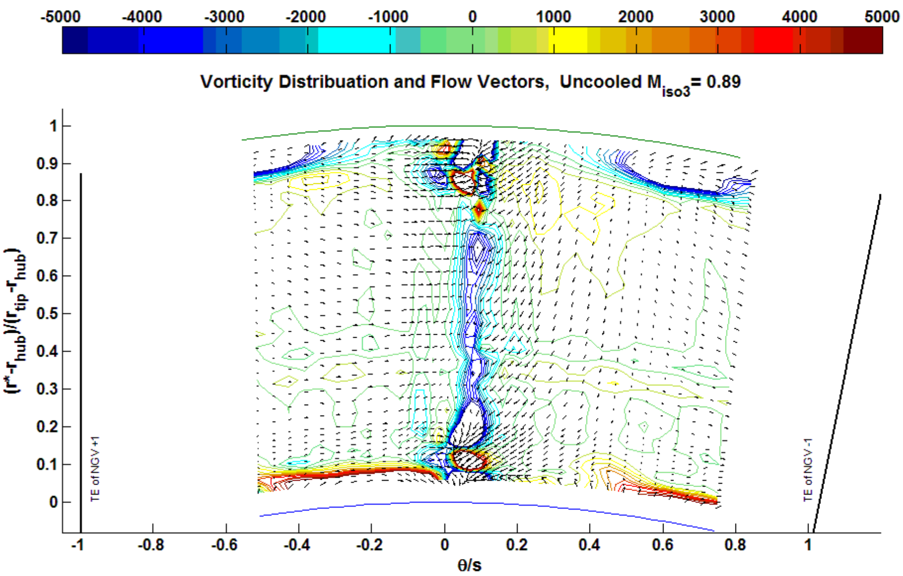

Figure 5-10: Vorticity distribution, uncooled vane

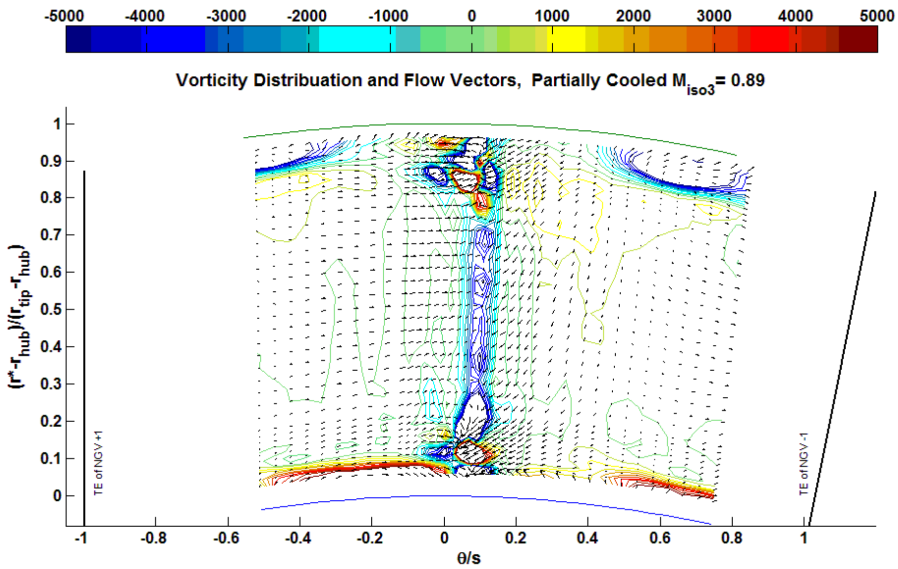

Figure 5-11: Vorticity distribution, partially cooled vane

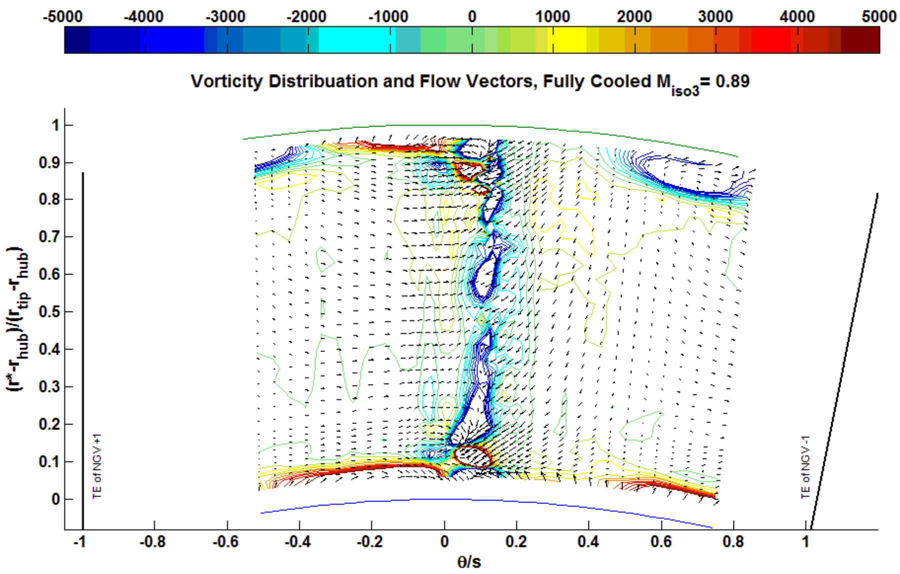

Figure 5-12: Vorticity distribution, fully cooled vane

The vorticity distributions for all three cooling configurations share some similar characteristics. High vorticities are found in the hub, tip, and trailing edge regions. Vorticities are generally positive near the hub and negative near the tip (though in the fully cooled vane there is also a region of positive vorticity near the trailing edge in the tip). The vorticities in the trailing edge region are mostly negative, though close to the hub and tip in the trailing edge for all configurations there are regions where positive and negative vortices meet (these meeting points occur around 10% and 90% span). Comparing the vorticity distributions to the kinetic energy loss coefficient distribution plots in section 5.3, it can be seen that areas of high vorticity tend to be areas of high losses. This makes sense, as high vorticity indicates the changing flow conditions that lead to losses in a turbine.

It is also worth noting that the fully cooled vane has more areas of high vorticity than the partially cooled and uncooled cases. The area of high vorticity in the trailing edge is wider, and the concentration of high vorticity near the tip is denser than in the other cases. Also, more vorticity can be observed away from the hub, tip, and trailing edge regions for the fully cooled vane than for the other cooling configurations.

5.4.2 Radial and Circumferential Vorticity

The radial and circumferential components of the vorticity have not been computed for this study, as they cannot be calculated directly from the experimental data. To do this, measurements would have to be taken in multiple axial planes, and the measurement sets used in this study include just one axial plane. However, the values of radial and circumferential vorticity can be estimated using the incompressible Helmholtz equation (Gregory-Smith, Graves, and Walsh 1988):

$$\vec{v} \times \omega = \frac{1}{\rho} \nabla p_0$$

Where p_0 is the total pressure and ρ is the density. The y- and z-components of this relation are:

$$V_x \omega_z - V_z \omega_x = \frac{1}{\rho} \frac{\partial p_0}{\partial y}$$

and

$$V_x \omega_y - V_y \omega_x = \frac{1}{\rho} \frac{\partial p_0}{\partial z}$$

The y-component of this relation can be used to calculate the radial component of the vorticity and the z-component can be used to calculate the circumferential component of the vorticity. Before these calculations can take place, it is necessary to compute the x-component of the velocity. With the magnitude, y-component, and z-component of velocity already determined, the x-component of velocity can be calculated by:

$$V_x = \sqrt{V^2 - V_y{}^2 - V_z{}^2}$$

The differentials in the equations above can be estimated using the gradient function of Matlab. Once these differential values have been calculated, the radial and circumferential values of vorticity can be determined.

6 UNCERTAINTY ANALYSIS

Uncertainties were estimated using the method developed by Kline and McClintock (1953). This method states that if the result R is a function of several independent variables $x_1, x_2, x_3, \ldots, x_n$ such that $R = R(x_1, x_2, x_3, \ldots x_n)$ and $w_1, w_2, w_3, \ldots, w_n$ are the uncertainties in the independent variables, the uncertainty in the result w_R can be determined by:

$$w_R = \sqrt{\left(\frac{\partial R}{\partial x_1} w_1\right)^2 + \left(\frac{\partial R}{\partial x_2} w_2\right)^2 + \left(\frac{\partial R}{\partial x_3} w_3\right)^2 + \cdots + \left(\frac{\partial R}{\partial x_n} w_n\right)^2}$$

The formula above only applies for uncertainties calculated with the same odds, meaning that the uncertainty of each independent variable must be stated with the same confidence interval. It is assumed throughout this analysis that the uncertainties of each of the independent variables are stated with the same odds.

6.1 Kinetic Energy Loss Coefficient Uncertainty

6.1.1 Fully Cooled and Partially Cooled Cases

The raw data values used in the uncertainty analysis include the five pressure values collected by the 5-hole probe $(p_1, p_2, p_3, p_4, p_5)$ as well as the settling chamber pressure, p_{sc}, and the total pressure of the coolant air, p_{cool}. The upstream hub static pressure measurements taken between the spanwise coordinates of -4.52° and $+0.0^{\circ}$ (five total data sets) are averaged to determine p_{21s}, the average upstream static pressure value used in calculations. The uncertainty analysis also uses the total temperature in the settling chamber, T and the total pressure, temperature and relative humidity factor (p_{mf}, T_{mf}, and rh_{mf}, respectively) of the mainstream flow measured at MF1, which is located just after the SV3 and SV4 valves and can be seen in the air supply schematic diagram. Finally, the uncertainty analysis includes the mass flow of the coolant air, $\dot{m}_c$ and the mass flow of the mainstream, $\dot{m}_m$. The first step in the uncertainty analysis was to determine the systematic and random uncertainties of each of the relevant measured values.

The measured pressures were subject to two different sources of systematic uncertainty—the inaccuracy of the barometer, and the inaccuracy of the pressure scanners. The PSI 9116 pressure scanner has an accuracy of ±0.05% of its full scale corresponding to ±51.75Pa and ±103.5Pa respectively for the relevant channels. In this uncertainty analysis, the maximum uncertainty of ±103.5Pa was used for all collected pressures in order to determine the maximum uncertainty of the overall loss measurements. The Solartron barometer has an accuracy of ±0.01% of its full scale, which corresponds to ±11.5 Pa. The overall systematic uncertainty of the pressure values was determined by:

$$wp_{sys} = \sqrt{{wp_{PSI}}^2 + {wp_{baro}}^2}$$

which leads to a systematic uncertainty of ±104.1 Pa for all measured pressure values.

The pressure scanner system functions such that, at each measurement point, 20 different values are measured, and the averages of these values are taken as the data value for that location. The random uncertainty for each of the pressure values, excluding p_{mf}, was then calculated during data collection by taking the standard deviation of the 20 values collected at each measurement point. The total uncertainty for the pressure values was then calculated by:

$$wp = \sqrt{{wp_{sys}}^2 + {wp_{ran}}^2}$$

The uncertainty value for p_{21s} is determined as follows:

$$wp_{21s} = \sqrt{\left(\frac{1}{5}wp_{20s,1}\right)^2 + \left(\frac{1}{5}wp_{20s,2}\right)^2 + \left(\frac{1}{5}wp_{20s,3}\right)^2 + \left(\frac{1}{5}wp_{20s,4}\right)^2 + \left(\frac{1}{5}wp_{20s,5}\right)^2}$$

where $wp_{20s,1} \dots wp_{20s,5}$ represent the systematic and random uncertainties for each of the five pressure measurements included in the average calculation to determine p_{21s}. The systematic and random uncertainties for these values are determined using the same methods described above.

The thermometer used to measure the temperature in the settling chamber has an accuracy of ±0.4˚ at 50˚C. Though the experiments take place at 30˚C, the 50˚C uncertainty value was treated as the systematic uncertainty for the settling chamber temperature in order to capture the maximum uncertainty in the overall measurements. The random uncertainty was calculated by taking the standard deviation of the full set of temperature data. The total uncertainty for the settling chamber temperature was then calculated by:

$$wT = \sqrt{{wT_{sys}}^2 + {wT_{ran}}^2}$$

The random uncertainties for p_{mf}, T_{mf}, and rh_{mf} were determined by taking the standard deviation of each of the full measurement sets. The systematic uncertainties in these values caused by the experimental equipment are unknown.

The random uncertainties for each of the measured mass flows, $\dot{m}_m$ and $\dot{m}_c$, were determined by taking the standard deviation of each of the full measurement sets. The systematic uncertainty caused by the coolant air mass flow controllers is ±0.1% of the full scale of 180 kg/h, corresponding to $\pm 5 * 10^{-5}$ kg/s. The total uncertainty for the coolant air mass flow can then be calculated by:

$$w\dot{m}_c = \sqrt{w\dot{m}_{c,sys}^{\ 2} + w\dot{m}_{c,ran}^{\ 2}}$$

The systematic uncertainty of the mainstream mass flow measurement is unknown. A previous study by Fridh (2012) found the absolute uncertainty of the mainstream mass flow measurement to be ±0.6%, but as this value did not distinguish between systematic and random uncertainties it was decided to use just the random uncertainty of the mass flow data set.

Table 6-1 summarizes the systematic and random uncertainties in the data measurements used:

Table 6-1: Systematic and random uncertainties of raw data

Data Value	Systematic Uncertainty	Random Uncertainty
p_1, p_2, p_3, p_4, p_5 (5-hole probe data)	±104.1 Pa	20 values measured then averaged at each measurement point, standard deviation of these values is logged during data collection
p_{sc} (settling chamber pressure)	±104.1 Pa	
p_{cool} (total pressure of cooling air)	±104.1 Pa	
Upstream hub static pressure between -4.52˚ and 0.0˚ (5 total pressure measurements)	±104.1 Pa for each	
p_{mf} (total pressure at MF1)	unknown	Standard deviation of data set
T_{mf} (temperature at MF1)	unknown	Standard deviation of data set
rh_{mf} (relative humidity at MF1)	unknown	Standard deviation of data set
T (settling chamber temperature)	±0.4°C	Standard deviation of data set
$\dot{m}_c$ (mass flow of coolant air)	$\pm 5 * 10^{-5}$ kg/s	Standard deviation of data set
$\dot{m}_m$ (mass flow of mainstream)	unknown	Standard deviation of data set

Once the uncertainties were determined for the relevant collected data, the analysis was continued by the uncertainty in the kinetic energy loss coefficient. The kinetic energy loss coefficient is calculated as described in section 5.3, and the uncertainties in *Y*, p_{30s}, p_{30}, p_{20}, and p_{cool} must all be determined in order to determine the uncertainty in this value.

Y is the ratio of the coolant air mass flow to the mainstream mass flow, and can be calculated by:

$$Y = \frac{\dot{m}_c}{\dot{m}_m}$$

The uncertainty in *Y* can be calculated by:

$$wY = \sqrt{\left(\frac{\partial Y}{\partial \dot{m}_c} w\dot{m}_c\right)^2 + \left(\frac{\partial Y}{\partial \dot{m}_m} w\dot{m}_m\right)^2}$$

where

$$\frac{\partial Y}{\partial \dot{m}_c} = \frac{1}{\dot{m}_m}$$

and

$$\frac{\partial Y}{\partial \dot{m}_m} = \frac{-\dot{m}_c}{\dot{m}_m^{\;2}}$$

P_{20} is calculated by the formula $p_{20} = (p_{sc} - p_{21s}) * p_n + p_{21s}$, where p_n is a scaling value used to correct for the inlet pressure gradient that the settling chamber pressure p_{sc} does not reflect. The uncertainty of p_{20} was calculated by:

$$wp_{20} = \sqrt{\left(\frac{\partial p_{20}}{\partial p_{sc}} wp_{sc}\right)^2 + \left(\frac{\partial p_{20}}{\partial p_{21s}} wp_{21s}\right)^2}$$

where

$$\frac{\partial p_{20}}{\partial p_{sc}} = p_n$$

and

$$\frac{\partial p_{20}}{\partial p_{21s}} = (1 - p_n)$$

Total and static pressures downstream of the flow, p_{30} and p_{30s} respectively, are calculated using an iterative approach using calibration values for the probe head. Total pressure is calculated through the formula:

$$p_{30} = k_1(p_1 - p_{ave}) + p_1$$

In this formula, p_1 is the pressure measured by the central hole in the 5-hole probe, while p_{ave} is the average of the pressures measured by the four other holes in the probe. The constant k_1 is calculated based on the probe head calibration, and this value changes in each iterative step until convergence.

The uncertainty in p_{ave} is calculated by:

$$wp_{ave} = \sqrt{\left(\frac{1}{4} wp_2\right)^2 + \left(\frac{1}{4} wp_3\right)^2 + \left(\frac{1}{4} wp_4\right)^2 \left(\frac{1}{4} wp_5\right)^2}$$

where $wp_2 \ldots wp_5$ represent the systematic and random uncertainties for each of the four pressure measurements included in the average calculation to determine p_{ave}.

The uncertainty in the total pressure value is calculated by:

$$wp_{30} = \sqrt{\left(\frac{\partial p_{30}}{\partial p_{ave}} wp_{ave}\right)^2 + \left(\frac{\partial p_{30}}{\partial p_1} wp_1\right)^2}$$

where

$$\frac{\partial p_{30}}{\partial p_{ave}} = -k_1$$

and

$$\frac{\partial p_{30}}{\partial p_1} = k_1 + 1$$

Static pressure is calculated through the formula:

$$p_{30s} = p_{30} - k_2(p_1 - p_{ave})$$

where k_2 is another constant calculated based on the probe head calibration, and changes in each iterative step until convergence.

The uncertainty in the static pressure value is calculated by:

$$wp_{30s} = \sqrt{\left(\frac{\partial p_{30s}}{\partial p_{ave}} wp_{ave}\right)^2 + \left(\frac{\partial p_{30s}}{\partial p_1} wp_1\right)^2 + \left(\frac{\partial p_{30s}}{\partial p_{30}} wp_{30}\right)^2}$$

where

$$\frac{\partial p_{30s}}{\partial p_{ave}} = k_2$$

$$\frac{\partial p_{30s}}{\partial p_1} = -k_2$$

and

$$\frac{\partial p_{30s}}{\partial p_{30}} = 1$$

With the uncertainties in *Y*, p_{30}, p_{30s}, p_{20}, and p_{cool} all calculated, the uncertainty in the kinetic energy loss coefficient can be calculated as follows:

$$w\zeta_{kin} = \sqrt{\left(\frac{\partial \zeta_{kin}}{\partial Y} wY\right)^2 + \left(\frac{\partial \zeta_{kin}}{\partial p_{30}} wp_{30}\right)^2 + \left(\frac{\partial \zeta_{kin}}{\partial p_{30s}} wp_{30s}\right)^2 + \left(\frac{\partial \zeta_{kin}}{\partial p_{20}} wp_{20}\right)^2 + \left(\frac{\partial \zeta_{kin}}{\partial p_{cool}} wp_{cool}\right)^2}$$

With the differentials evaluated as:

$$\frac{\partial \zeta_{kin}}{\partial Y} = \frac{[-\left[1-\left(\frac{p_{30s}}{p_{30}}\right)^{\frac{k-1}{k}}\right] * \left(1-\left(\frac{p_{30s}}{p_{20}}\right)^{\frac{k-1}{k}} + Y\left[1-\left(\frac{p_{30s}}{p_{cool}-p_{dp}}\right)^{\frac{k-1}{k}}\right]\right) + \left[1-\left(\frac{p_{30s}}{p_{cool}-p_{dp}}\right)^{\frac{k-1}{k}}\right] * \left((1+Y)\left[1-\left(\frac{p_{30s}}{p_{30}}\right)^{\frac{k-1}{k}}\right]\right)]}{\left(1-\left(\frac{p_{30s}}{p_{20}}\right)^{\frac{k-1}{k}} + Y\left[1-\left(\frac{p_{30s}}{p_{cool}-p_{dp}}\right)^{\frac{k-1}{k}}\right]\right)^2}$$

$$\frac{\partial \zeta_{kin}}{\partial p_{30}} = \frac{-(1+Y)}{1-\left(\frac{p_{30s}}{p_{20}}\right)^{\frac{k-1}{k}} + Y\left[1-\left(\frac{p_{30s}}{p_{cool}-p_{dp}}\right)^{\frac{k-1}{k}}\right]} * \frac{\frac{k-1}{k} p_{30s}{}^{\frac{k-1}{k}}}{p_{30}{}^{\left(\frac{k-1}{k}+1\right)}}$$

$$\frac{\partial \zeta_{kin}}{\partial p_{30s}} = \frac{[-\left(1-\left(\frac{p_{30s}}{p_{20}}\right)^{\frac{k-1}{k}} + Y\left[1-\left(\frac{p_{30s}}{p_{cool}-p_{dp}}\right)^{\frac{k-1}{k}}\right]\right) * \left(-(1+Y) * \frac{k-1}{k} * \frac{p_{30s}{}^{\left(\frac{k-1}{k}-1\right)}}{p_{30}{}^{\frac{k-1}{k}}}\right) + \left((1+Y)\left[1-\left(\frac{p_{30s}}{p_{30}}\right)^{\frac{k-1}{k}}\right]\right) * \left(\frac{-\frac{k-1}{k} p_{30s}{}^{\left(\frac{k-1}{k}-1\right)}}{p_{20}{}^{\frac{k-1}{k}}} - \frac{Y\left(\frac{k-1}{k}\right) p_{30s}{}^{\left(\frac{k-1}{k}-1\right)}}{(p_{cool}-p_{dp})^{\frac{k-1}{k}}}\right)]}{\left(1-\left(\frac{p_{30s}}{p_{20}}\right)^{\frac{k-1}{k}} + Y\left[1-\left(\frac{p_{30s}}{p_{cool}-p_{dp}}\right)^{\frac{k-1}{k}}\right]\right)^2}$$

$$\frac{\partial \zeta_{kin}}{\partial p_{20}} = \frac{(1+Y)\left[1-\left(\frac{p_{30s}}{p_{30}}\right)^{\frac{k-1}{k}}\right]}{\left(1-\left(\frac{p_{30s}}{p_{20}}\right)^{\frac{k-1}{k}} + Y\left[1-\left(\frac{p_{30s}}{p_{cool}-p_{dp}}\right)^{\frac{k-1}{k}}\right]\right)^2} * \frac{\frac{k-1}{k} p_{30s}{}^{\frac{k-1}{k}}}{p_{20}{}^{\left(\frac{k-1}{k}+1\right)}}$$

$$\frac{\partial \zeta_{kin}}{\partial p_{cool}} = \frac{(1+Y)\left[1-\left(\frac{p_{30s}}{p_{30}}\right)^{\frac{k-1}{k}}\right]}{\left(1-\left(\frac{p_{30s}}{p_{20}}\right)^{\frac{k-1}{k}} + Y\left[1-\left(\frac{p_{30s}}{p_{cool}-p_{dp}}\right)^{\frac{k-1}{k}}\right]\right)^2} * \frac{Y * \frac{k-1}{k} p_{30s}{}^{\frac{k-1}{k}}}{(p_{cool}-p_{dp})^{\left(\frac{k-1}{k}+1\right)}}$$

6.1.2 Uncooled Case

When the film cooling holes in the NGV's are all blocked, the coolant mass flow $\dot{m}_c$ is 0 kg/s, thereby making the mass flux ratio Y equal to 0 as well. This changes the equation used to calculate the kinetic energy loss coefficient, as described in section 5.3. The equations used for calculating the uncertainty of the kinetic energy loss coefficient also change for the uncooled case. The uncertainty can be calculated by:

$$w\zeta_{kin} = \sqrt{\left(\frac{\partial \zeta_{kin}}{\partial p_{30}} wp_{30}\right)^2 + \left(\frac{\partial \zeta_{kin}}{\partial p_{30s}} wp_{30s}\right)^2 + \left(\frac{\partial \zeta_{kin}}{\partial p_{20}} wp_{20}\right)^2}$$

where

$$\frac{\partial \zeta_{kin}}{\partial p_{30}} = \frac{\frac{-(k-1)}{k} * \frac{p_{30s}^{\frac{k-1}{k}}}{p_{30}^{\left(\frac{k-1}{k}+1\right)}}}{1-\left(\frac{p_{30s}}{p_{20}}\right)^{\frac{k-1}{k}}}$$

$$\frac{\partial \zeta_{kin}}{\partial p_{30s}} = \frac{[\left(\frac{k-1}{k} * \frac{p_{30s}^{\left(\frac{k-1}{k}-1\right)}}{p_{30}^{\frac{k-1}{k}}} - \frac{k-1}{k} * \frac{p_{30s}^{\left(\frac{k-1}{k}-1\right)}}{p_{20}^{\frac{k-1}{k}}}\right) * \left(1-\left(\frac{p_{30s}}{p_{20}}\right)^{\frac{k-1}{k}}\right) - \left(\frac{-(k-1)}{k} * \frac{p_{30s}^{\left(\frac{k-1}{k}-1\right)}}{p_{20}^{\frac{k-1}{k}}}\right) * \left(\left(\frac{p_{30s}}{p_{30}}\right)^{\frac{k-1}{k}} - \left(\frac{p_{30s}}{p_{20}}\right)^{\frac{k-1}{k}}\right)]}{\left(1-\left(\frac{p_{30s}}{p_{20}}\right)^{\frac{k-1}{k}}\right)^2}$$

and

$$\frac{\partial \zeta_{kin}}{\partial p_{20}} = \frac{\frac{k-1}{k} * \frac{p_{30s}^{\frac{k-1}{k}}}{p_{20}^{\left(\frac{k-1}{k}+1\right)}} * \left(1-\left(\frac{p_{30s}}{p_{30}}\right)^{\frac{k-1}{k}}\right)}{\left(1-\left(\frac{p_{30s}}{p_{20}}\right)^{\frac{k-1}{k}}\right)^2}$$

The uncertainties in p_{30}, p_{30s}, and p_{20} are calculated in the same way as in the cooled and partially cooled cases, as described in section 6.1.1.

6.1.3 Results and Discussion

Figures 6-1, 6-2, and 6-3 display a contour plot of uncertainty in the kinetic energy loss coefficient for the different cooling conditions.

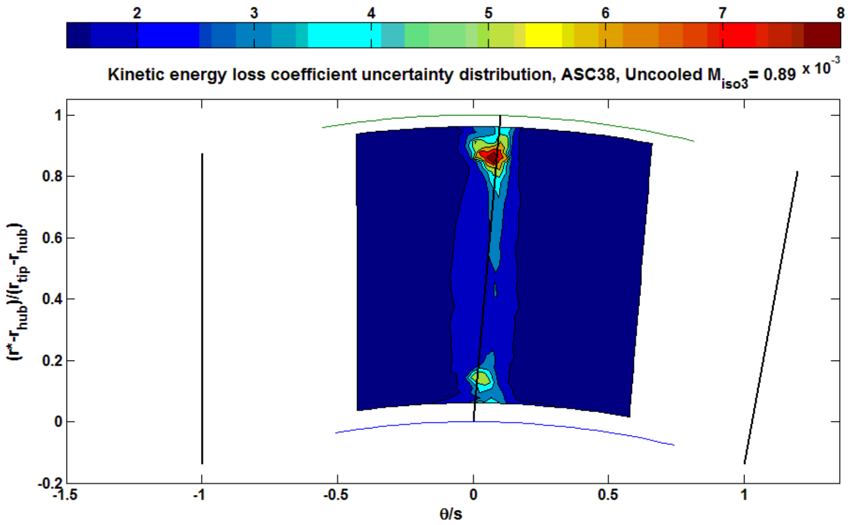

Figure 6-1: Loss coefficient uncertainty distribution, uncooled vane

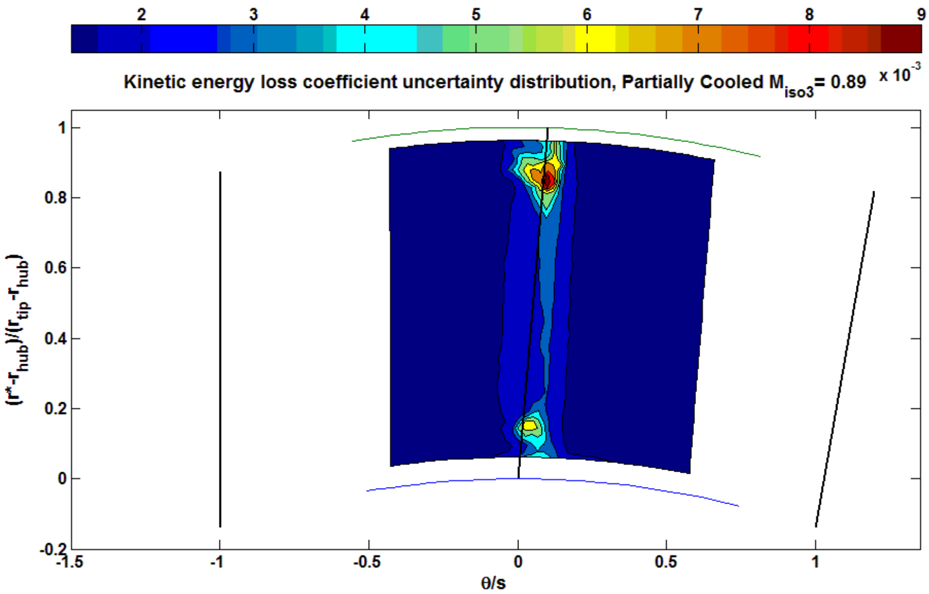

Figure 6-2: Loss coefficient uncertainty distribution, partially cooled vane

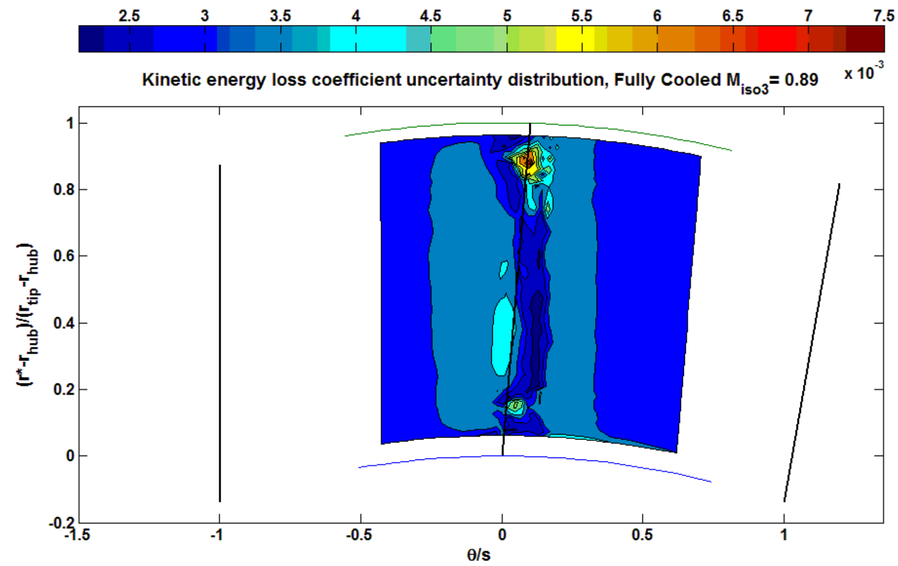

Figure 6-3: Loss coefficient uncertainty distribution, fully cooled vane

As in the loss coefficient distributions shown in Figures 5-6, 5-7, and 5-8, the uncertainty distributions for the uncooled and partially cooled configurations closely resemble each other, while the distribution for the fully cooled case differs. For the uncooled and partially cooled configurations, uncertainty is low in all regions except a band through the wake region. In this region, there are areas of especially high uncertainty close to the hub and tip. For the fully cooled vane, uncertainty values are higher throughout the entire measurement grid, with a thick band of high uncertainty values around the hub. The regions of especially high uncertainty near the hub and tip are smaller for the fully cooled case than for the other two cooling configurations.

Comparing the vorticity plots in Figures 5-10, 5-11, and 5-12 to the uncertainty distributions, a correlation can be seen between the areas of high vorticity and the areas of high uncertainty. Especially high uncertainty values can be found in areas where positive and negative vortices meet, such as in the wake region close to the hub and tip. This makes sense, as these are areas with rapid fluctuations and unsteady flow conditions. The overall higher values of uncertainty for the fully cooled configuration can be explained by the higher vorticity throughout the measurement grid for this case.

6.2 Mass-Averaged Loss Coefficient Uncertainty

After calculating the uncertainty found in the kinetic energy loss coefficient, the next step was to calculate the uncertainty in the mass-averaged kinetic energy loss coefficient. In order to calculate the uncertainty in this value, the uncertainties in the density, area, and axial velocity values must be determined.

The area cell A_n for each measurement point is calculated using the method described in section 5.2. The equations used for calculating uncertainty in the area for central cells, top and bottom cells, side cells, and corner cells are each slightly different.

For central, top, and bottom cells, the uncertainty in the area calculations is calculated by the same formula, though the differentials used in each case differ. The equation used to calculate the uncertainty in these area cells is:

$$wA_n = \sqrt{\left(\frac{\partial A_n}{\partial \Phi_{m+1}} w\Phi_{m+1}\right)^2 + \left(\frac{\partial A_n}{\partial \Phi_{m-1}} w\Phi_{m-1}\right)^2}$$

For the central area cells, the following differentials are used:

$$\frac{\partial A_n}{d\Phi_{m+1}} = \frac{1}{4}\left[\left(r_n + \frac{r_{n+1} - r_n}{2}\right)^2 - \left(r_n - \frac{r_n - r_{n-1}}{2}\right)^2\right]$$

$$\frac{\partial A_n}{d\Phi_{m-1}} = -\frac{1}{4}\left[\left(r_n + \frac{r_{n+1} - r_n}{2}\right)^2 - \left(r_n - \frac{r_n - r_{n-1}}{2}\right)^2\right]$$

For top cells, the following differentials are used:

$$\frac{\partial A_n}{\partial \Phi_{m+1}} = \frac{1}{4}\left[(r_n)^2 - \left(r_n - \frac{r_n - r_{n-1}}{2}\right)^2\right]$$

$$\frac{\partial A_n}{\partial \Phi_{m-1}} = -\frac{1}{4}\left[(r_n)^2 - \left(r_n - \frac{r_n - r_{n-1}}{2}\right)^2\right]$$

For bottom cells, the following differentials are used:

$$\frac{\partial A_n}{\partial \Phi_{m+1}} = \frac{1}{4}\left[\left(r_n + \frac{r_{n+1} - r_n}{2}\right)^2 - (r_n)^2\right]$$

$$\frac{\partial A_n}{\partial \Phi_{m-1}} = -\frac{1}{4}\left[\left(r_n + \frac{r_{n+1} - r_n}{2}\right)^2 - (r_n)^2\right]$$

The uncertainty in area calculations for the edge cells is calculated differently for both the left and right cells. The uncertainty in area for the cells on the left edge of the grid, including both corners of the left edge of the grid, is calculated with the following equation:

$$wA_n = \sqrt{\left(\frac{\partial A_n}{\partial \Phi_m} w\Phi_m\right)^2 + \left(\frac{\partial A_n}{\partial \Phi_{m-1}} w\Phi_{m-1}\right)^2}$$

The differentials used when calculating the uncertainty of the non-corner edge cells and the corner edge cells differ. The following differentials are used for the non-corner edge cells:

$$\frac{\partial A_n}{\partial \Phi_m} = \frac{1}{4}\left[\left(r_n + \frac{r_{n+1} - r_n}{2}\right)^2 - \left(r_n - \frac{r_n - r_{n-1}}{2}\right)^2\right]$$

$$\frac{\partial A_n}{\partial \Phi_{m-1}} = -\frac{1}{4}\left[\left(r_n + \frac{r_{n+1} - r_n}{2}\right)^2 - \left(r_n - \frac{r_n - r_{n-1}}{2}\right)^2\right]$$

The following differentials are used for calculating the uncertainty of the top left corner cell:

$$\frac{\partial A_n}{\partial \Phi_m} = \frac{1}{4}\left[(r_n)^2 - \left(r_n - \frac{r_n - r_{n-1}}{2}\right)^2\right]$$

$$\frac{\partial A_n}{\partial \Phi_{m-1}} = -\frac{1}{4}\left[(r_n)^2 - \left(r_n - \frac{r_n - r_{n-1}}{2}\right)^2\right]$$

The following differentials are used for calculating the uncertainty of the bottom left corner cell:

$$\frac{\partial A_n}{\partial \Phi_m} = \frac{1}{4}\left[\left(r_n + \frac{r_{n+1} - r_n}{2}\right)^2 - (r_n)^2\right]$$

$$\frac{\partial A_n}{\partial \Phi_{m-1}} = -\frac{1}{4}\left[\left(r_n + \frac{r_{n+1} - r_n}{2}\right)^2 - (r_n)^2\right]$$

The uncertainty in area for the cells on the right edge of the grid, including both corners on the right edge of the grid, is calculated with the following equation:

$$wA_n = \sqrt{\left(\frac{\partial A_n}{\partial \Phi_{m+1}} w\Phi_{m+1}\right)^2 + \left(\frac{\partial A_n}{\partial \Phi_m} w\Phi_m\right)^2}$$

The differentials used when calculating the uncertainty of the non-corner edge cells and the corner edge cells differ. The following differentials are used for the non-corner edge cells:

$$\frac{\partial A_n}{\partial \Phi_{m+1}} = \frac{1}{4}\left[\left(r_n + \frac{r_{n+1} - r_n}{2}\right)^2 - \left(r_n - \frac{r_n - r_{n-1}}{2}\right)^2\right]$$

$$\frac{\partial A_n}{\partial \Phi_m} = -\frac{1}{4}\left[\left(r_n + \frac{r_{n+1} - r_n}{2}\right)^2 - \left(r_n - \frac{r_n - r_{n-1}}{2}\right)^2\right]$$

The following differentials are used for calculating the uncertainty of the top right corner cell:

$$\frac{\partial A_n}{\partial \Phi_{m+1}} = \frac{1}{4}\left[(r_n)^2 - \left(r_n - \frac{r_n - r_{n-1}}{2}\right)^2\right]$$

$$\frac{\partial A_n}{\partial \Phi_m} = -\frac{1}{4}\left[(r_n)^2 - \left(r_n - \frac{r_n - r_{n-1}}{2}\right)^2\right]$$

The following differentials are used for calculating the uncertainty of the bottom right corner cell:

$$\frac{\partial A_n}{\partial \Phi_{m+1}} = \frac{1}{4}\left[\left(r_n + \frac{r_{n+1} - r_n}{2}\right)^2 - (r_n)^2\right]$$

$$\frac{\partial A_n}{\partial \Phi_m} = -\frac{1}{4}\left[\left(r_n + \frac{r_{n+1} - r_n}{2}\right)^2 - (r_n)^2\right]$$

These calculations for the uncertainty in the area measurements all require knowledge of the uncertainty in the pitchwise angle Φ_m. This angle is calculated from the position of the linear unit by using a set of geometric relations. The linear unit has a systematic uncertainty of ±0.02 mm. The position of the linear unit is first used to calculate an angle which is corrected in two different ways in order to obtain the pitchwise angle Φ_m. This first angle is calculated by:

$$\theta = sin^{-1}\left(\frac{x + x_{corr}}{r_{cart}}\right) - (21 - 18.54)$$

In this equation, x_{corr} is added to the horizontal position of the unit to correct for a small angle difference of 0.15˚ at the zero point for the linear unit and r_{cart} is the radius of the cylindrical drive pin for the traverse cart. The uncertainty of this angle can be calculated by:

$$w\theta = \frac{\partial\theta}{\partial x} wx$$

where

$$\frac{\partial\theta}{\partial x} = \frac{1}{r\sqrt{1 - \left(\frac{x + x_{corr}}{r_{cart}}\right)^2}}$$

The angle θ is then corrected due to the geometric properties of the test sector using the following equation:

$$\theta_{corr} = \theta + (19.5 - 16.6) - 9.18$$

From this equation it can be seen that $w\theta_{corr} = w\theta$. The angular position of the probe head Φ_m is then calculated using the following equation, where $\Delta\theta_{probe}$ is a calculated value derived from the geometric properties of the probe:

$$\Phi_m = \theta_{corr} - \Delta\theta_{probe}$$

In the equation above, $\Delta\theta_{probe}$ is a correction that is applied due to the probe not being set directly in the tangential plane—instead, it is offset from the tangential plane by an angle of 18.6˚, which impacts the pitchwise angle that the probe head is at relative to the angular position of the traverse cart. The uncertainty in the angular position of the probe head can then be calculated by:

$$w\Phi_m = w\theta_{corr}$$

The absolute axial velocity, $c_{ax,i}$ at each grid point is calculated by the following equations:

$$a = \sqrt{kR_g T_s}$$

$$c = Ma$$

$$c_{ax} = c * cos\gamma$$

where γ is the axial flow angle and T_s is the static temperature in the settling chamber, calculated by:

$$T_s = T\left(\frac{p_{30s}}{p_{30}}\right)^{\frac{k-1}{k}}.$$

The uncertainty in the axial velocity is calculated by:

$$wc_{ax} = \frac{\partial c_{ax}}{\partial c} wc$$

where

$$\frac{\partial c_{ax}}{\partial c} = cos\gamma$$

$$wc = \sqrt{\left(\frac{\partial c}{\partial M} wM\right)^2 + \left(\frac{dc}{da} wa\right)^2}$$

$$\frac{\partial c}{\partial M} = a$$

and

$$\frac{\partial c}{\partial a} = M$$

In order to complete the calculation above, the uncertainty in the Mach number M and the uncertainty in the speed of sound a must be found. The Mach number downstream of the nozzle guide vanes is calculated using an iterative approach based on calibration values for the probe head. The Mach number is calculated through the formula:

$$M = \sqrt{\frac{2}{k-1}\left[\left(\frac{p_{30}}{p_{30s}}\right)^{\frac{k-1}{k}} - 1\right]}$$

Uncertainty in the Mach number can be evaluated as:

$$wM = \sqrt{\left(\frac{\partial \text{M}}{\partial P_{30}} wp_{30}\right)^2 + \left(\frac{\partial \text{M}}{\partial \text{P}_{30s}} wp_{30s}\right)^2}$$

where

$$\frac{\partial \text{M}}{\partial p_{30}} = \frac{\sqrt{\frac{2}{k-1}}}{2\sqrt{\left(\frac{p_{30}}{p_{30s}}\right)^{\frac{k-1}{k}} - 1}} * \frac{k-1}{k} * \frac{p_{30}{}^{\left(\frac{k-1}{k}-1\right)}}{p_{30s}{}^{\frac{k-1}{k}}}$$

and

$$\frac{\partial \text{M}}{\partial p_{30s}} = \frac{\sqrt{\frac{2}{k-1}}}{2\sqrt{\left(\frac{p_{30}}{p_{30s}}\right)^{\frac{k-1}{k}} - 1}} * \frac{-(k-1)}{k} * \frac{p_{30}{}^{\frac{k-1}{k}}}{p_{30s}{}^{\left(\frac{k-1}{k}-1\right)}}$$

In order to calculate the uncertainty in the speed of sound wa, it is first necessary to find the uncertainty in the gas constant R_g as well as the uncertainty in the static temperature T_s.

The uncertainty in the static temperature can be calculated as:

$$wT_s = \sqrt{\left(\frac{\partial T_s}{\partial p_{30}} wp_{30}\right)^2 + \left(\frac{\partial T_s}{\partial p_{30s}} wp_{30s}\right)^2 + \left(\frac{\partial \text{T}_s}{\partial \text{T}} wT\right)^2}$$

where

$$\frac{\partial T_s}{\partial p_{30}} = \frac{T * \frac{-(k-1)}{k} * p_{30s}{}^{\frac{k-1}{k}}}{p_{30}{}^{\left(\frac{k-1}{k}-1\right)}}$$

$$\frac{\partial T_s}{\partial p_{30s}} = \frac{T * \frac{k-1}{k} * p_{30s}{}^{\left(\frac{k-1}{k}-1\right)}}{p_{30}{}^{\frac{k-1}{k}}}$$

and

$$\frac{\partial T_s}{\partial \text{T}} = \left(\frac{p_{30s}}{p_{30}}\right)^{\frac{k-1}{k}}$$

Calculating the uncertainty in the gas constant R_g is more complicated. The gas constant is calculated through the following set of equations:

$$p_{H20_{sat}} = e^{\left(12.03 - \left(\frac{4025}{t_{mf}+235}\right)\right)}$$

$$p_{H20} = p_{H20_{sat}} \left(\frac{rh_{mf}}{100}\right)$$

$$X = \frac{18.016}{28.97}\left(\frac{p_{H20}}{\frac{p_{mf}}{100} - p_{H20}}\right)$$

$$R_g = \frac{8314}{(1+X)}\left(\frac{1}{28.97} + \frac{X}{18.016}\right)$$

The uncertainty in $p_{H20_{sat}}$ can be calculated as:

$$wp_{H20_{sat}} = \frac{\partial p_{H20_{sat}}}{\partial t_{mf}} wt_{mf}$$

where

$$\frac{\partial p_{H20_{sat}}}{\partial t_{mf}} = \frac{4025}{(t_{mf}+235)^2} * e^{\left(12.03 - \left(\frac{4025}{t_{mf}+235}\right)\right)}$$

The uncertainty in p_{H20} is calculated as:

$$wp_{H20} = \sqrt{\left(\frac{\partial p_{H20}}{\partial p_{H20_{sat}}} wp_{H20_{sat}}\right)^2 + \left(\frac{\partial p_{H20}}{\partial rh_{mf}} wrh_{mf}\right)^2}$$

where

$$\frac{\partial p_{H20}}{\partial p_{H20_{sat}}} = \frac{rh_{mf}}{100}$$

and

$$\frac{\partial p_{H20}}{\partial rh_{mf}} = \frac{p_{H20_{sat}}}{100}$$

Next, the uncertainty in *X* can be evaluated by:

$$wX = \sqrt{\left(\frac{\partial X}{\partial p_{H20}} wp_{H20}\right)^2 + \left(\frac{\partial X}{\partial p_{mf}} wp_{mf}\right)^2}$$

where

$$\frac{\partial X}{\partial p_{H20}} = \frac{18.016}{28.97}\left(\frac{p_{mf}}{100\left(\frac{p_{mf}}{100} - p_{H20}\right)^2}\right)$$

and

$$\frac{\partial X}{\partial p_{mf}} = \frac{-18.016}{28.97}\left(\frac{p_{H20}}{100\left(\frac{p_{mf}}{100} - p_{H20}\right)^2}\right)$$

The uncertainty in R_g can then be found by:

$$wR_g = \frac{\partial R_g}{\partial X} wX$$

where

$$\frac{\partial R_g}{\partial X} = \frac{8314}{28.97(1+X)^2} + \frac{8314}{18.016(1+X)^2}$$

Once the uncertainty in the gas constant has been calculated, the uncertainty in the speed of sound can be evaluated by:

$$wa = \sqrt{(\frac{\partial a}{\partial T_s} wT_s)^2 + (\frac{\partial a}{\partial R_g} wR_g)^2}$$

where

$$\frac{\partial a}{\partial T_s} = \frac{\sqrt{kR_g}}{2\sqrt{T_s}}$$

and

$$\frac{\partial a}{\partial R_g} = \frac{\sqrt{kT_s}}{2\sqrt{R_g}}$$

Once the uncertainty in the speed of sound has been calculated, all values necessary for calculating the uncertainty in the axial velocity have been produced.

The next uncertainty value that must be calculated is the uncertainty in the density measurements. With the assumption of ideal gas behavior for air, density is calculated by:

$$\rho = \frac{p_{30s}}{R_g T_s}$$

The uncertainty in density is calculated by:

$$w\rho = \sqrt{(\frac{\partial \rho}{\partial p_{30s}} wp_{30s})^2 + (\frac{\partial \rho}{\partial R_g} wR_g)^2 + (\frac{\partial \rho}{\partial T_s} wT_s)^2}$$

where

$$\frac{\partial \rho}{\partial p_{30s}} = \frac{1}{R_g T_s}$$

$$\frac{\partial \rho}{\partial R_g} = \frac{-p_{30s}}{{R_g}^2 T_s}$$

and

$$\frac{\partial \rho}{\partial T_s} = \frac{-p_{30s}}{R_g {T_s}^2}$$

The uncertainties in p_{30s}, R_g, and T_s have already been calculated for other portions of the uncertainty analysis and therefore do not need to be re-evaluated in this case.

After calculating the uncertainties in density, area, axial velocity, and kinetic energy loss coefficient, these values must all be combined in order to determine the mass-averaged kinetic energy loss coefficients for the different types of cooling. Due to the presence of summations in both the numerator and denominator of the mass-averaging equation, the uncertainties in the numerator and denominator are first evaluated separately and then combined.

The uncertainty in the numerator of the mass-averaging equation can be calculated by:

$$wnum = \left[\sum_{i=1}^{r}\left(\left(\frac{\partial \mathrm{num}_i}{\partial \rho_i} w\rho_i\right)^2 + \left(\frac{\partial \mathrm{num}_i}{\partial A_i} wA_i\right)^2 + \left(\frac{\partial \mathrm{num}_i}{\partial c_{ax,i}} wc_{ax,i}\right)^2 + \left(\frac{\partial \mathrm{num}_i}{\partial \zeta_{kin,i}} w\zeta_{kin,i}\right)^2\right)\right]^{\frac{1}{2}}$$

where

$$\frac{\partial \mathrm{num}_i}{\partial \rho_i} = A_i c_{ax,i} \zeta_{kin,i}$$

$$\frac{\partial num_i}{\partial A_i} = \rho_i c_{ax,i} \zeta_{kin,i}$$

$$\frac{\partial num_i}{\partial c_{ax.i}} = \rho_i A_i \zeta_{kin,i}$$

and

$$\frac{\partial num_i}{\partial \zeta_{kin,i}} = \rho_i A_i c_{ax,i}$$

The uncertainty in the denominator of the mass-averaging equation can be calculated by:

$$wden = \left[\sum_{i=1}^{r}\left(\left(\frac{\partial \mathrm{den}_i}{\partial \rho_i} w\rho_i\right)^2 + \left(\frac{\partial \mathrm{den}_i}{\partial A_i} wA_i\right)^2 + \left(\frac{\partial \mathrm{den}_i}{\partial c_{ax,i}} wc_{ax,i}\right)^2\right)\right]^{\frac{1}{2}}$$

where

$$\frac{\partial \mathrm{den}_i}{\partial \rho_i} = A_i c_{ax,i}$$

$$\frac{\partial den_i}{\partial A_i} = \rho_i c_{ax,i}$$

and

$$\frac{\partial den_i}{\partial c_{ax.i}} = \rho_i A_i$$

The full uncertainty in the mass-averaged kinetic energy loss coefficients can then be calculated by:

$$w\zeta_{kin,avg} = \sqrt{(\frac{\partial\zeta_{kin,avg}}{\partial \mathrm{num}} wnum)^2 + (\frac{\partial\zeta_{kin,avg}}{\partial \mathrm{den}} wden)^2}$$

where

$$\frac{\partial\zeta_{kin,avg}}{\partial \mathrm{num}} = \frac{1}{den}$$

and

$$\frac{\partial\zeta_{kin,avg}}{\partial \mathrm{den}} = \frac{-num}{den^2}$$

6.2.1 Results and Discussion

Figures 6-4, 6-5, and 6-6 show the mass-averaged kinetic energy loss coefficient at each radial length, with error bars representing the uncertainty of the calculated value, for the uncooled, partially cooled, and fully cooled cases, respectively.

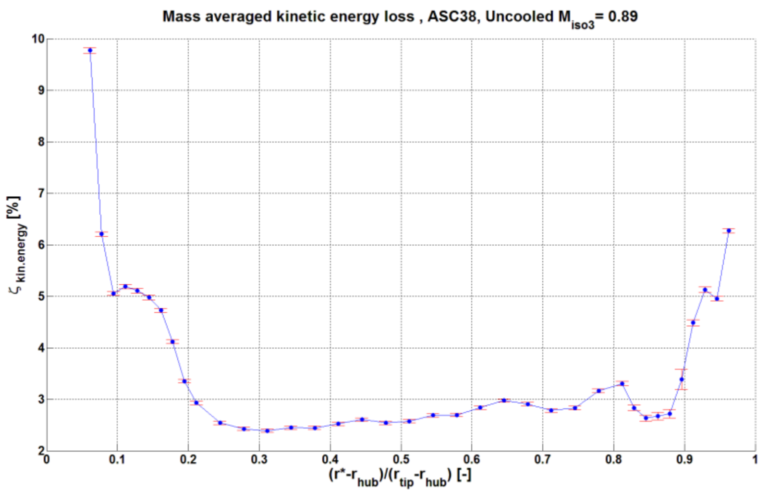

Figure 6-4: Mass-averaged loss coefficient with error bars, uncooled vane

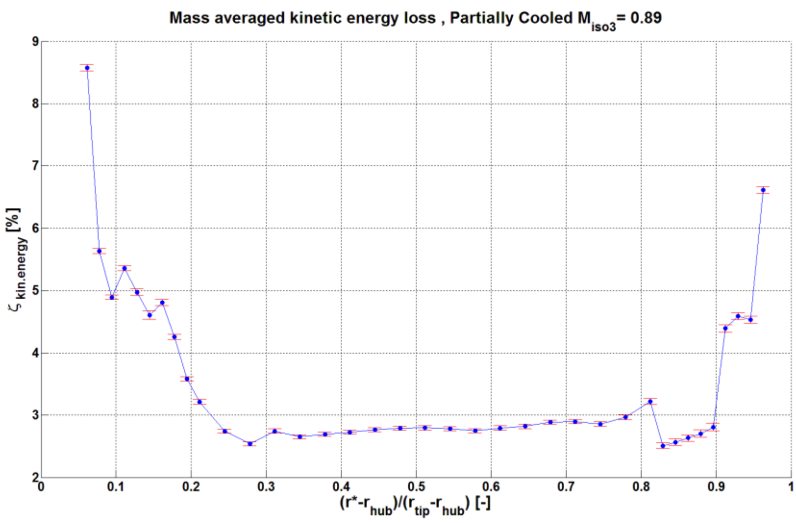

Figure 6-5: Mass-averaged loss coefficient with error bars, partially cooled vane

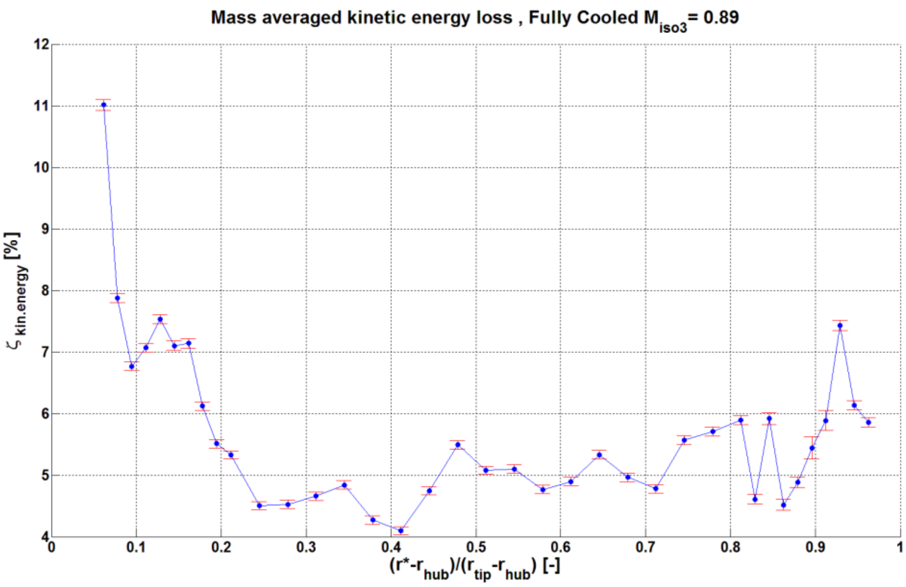

Figure 6-6: Mass-averaged loss coefficient with error bars, fully cooled vane

The mass-averaged loss values for all three cooling cases follow a similar distribution, with the highest loss coefficient values at radial lengths close to the hub, followed by radial lengths close to the tip while losses near the center of the vane are lower. The value of the mass-averaged loss coefficient is higher for the fully cooled vane than for the uncooled and partially cooled configurations. Table 6-1, which includes the average and maximum values of the mass-averaged loss coefficient, and Figure 6-7, which displays a comparison of the mass-averaged losses for each of the vane configurations, confirm these observed trends.

Table 6-2: Average, Maximum Mass-Averaged Loss Coefficient Values

Cooling Configuration	Maximum KE Loss Coefficient Value	Average KE Loss Coefficient Value
Uncooled Vane	11.01%	4.87%
Partially Cooled Vane	8.58%	2.93%
Fully Cooled Vane	9.77%	2.95%

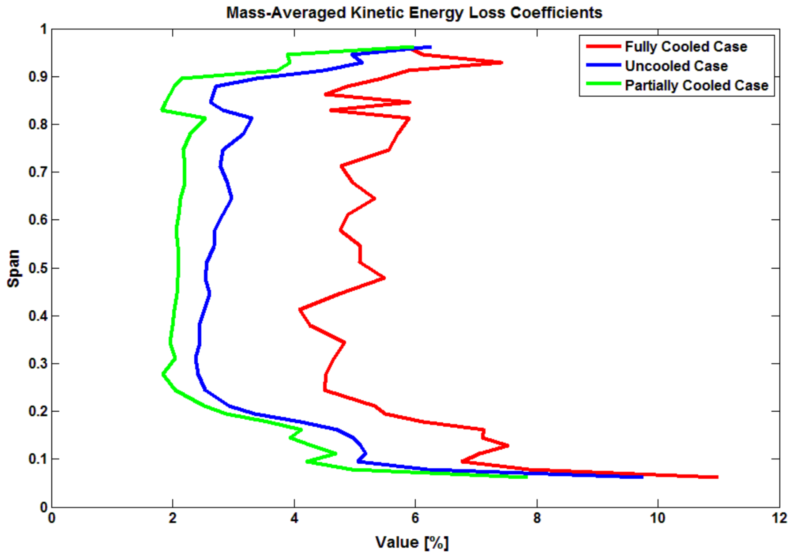

Figure 6-7: Comparison of mass-averaged losses for different cooling cases

As seen in Table 6-2, the average mass-averaged loss coefficients (calculated as the area between the loss curve and the y-axis) for the uncooled and partially cooled cases are nearly identical (2.97% for uncooled versus 2.95% for partially cooled), while that of the fully cooled vane is much higher at 4.87%. Though the general shape of the mass-averaged loss curve for the fully cooled case is similar to that of the uncooled and partially cooled cases, more fluctuations in the value can be observed and there is a decrease in losses at the radial length closest to the tip, which is not seen for the partially cooled and uncooled cases. These two differences from the curve shape seen for the uncooled and partially cooled cases probably result from increased flow interactions and mixing due to the higher blowing ratio in this cooling configuration.

Figure 6-8 shows a comparison of the uncertainties in the mass-averaged loss coefficient. It can be seen in this figure that at most radial lengths, the uncertainty in the uncooled and partially cooled cases is roughly the same. There are two places where this is not the case: at about 90% span the uncertainty in the uncooled case has a very large increase while the uncertainty for the partially cooled case increases only slightly. Around 10% span the uncertainty in the partially cooled case increases by more than that of the uncooled vane, but the differences between values is smaller here than at 90% span. The uncertainty in the fully cooled case follows the same general trend as the uncertainty in the uncooled case, with a relatively constant value throughout the span except for a large increase at 90% span and a much smaller increase around 10% span, though the magnitude of the uncertainty is larger in the fully cooled case.

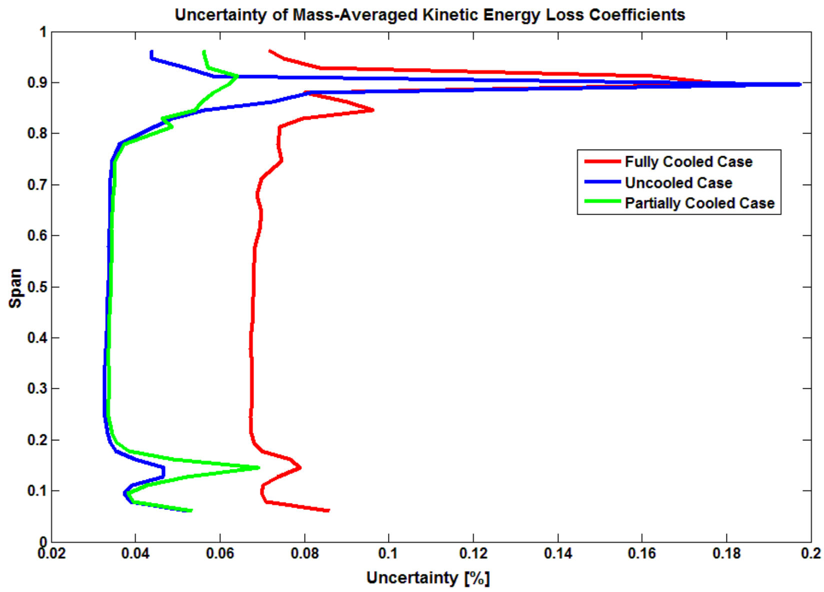

Figure 6-8: Uncertainty in mass-averaged losses for different cooling cases

Comparing the uncertainty curves to the vorticity distributions in Figures 5-10, 5-11, and 5-12, the increase in uncertainty seen for all configurations around 10% span and again around 90% span can be attributed to the meeting of clockwise and counterclockwise rotating vortices in the trailing edge region. The dramatically smaller increase in uncertainty at 90% span for the partially cooled case seems to be due to interactions between the mainstream flow and the coolant air in which secondary flow effects near the tip are reduced, thereby leading to smaller fluctuations and less unsteadiness in the flow field in this region.

Table 6-3 shows the average and maximum uncertainty in the mass-averaged kinetic energy loss coefficient for the three different cooling configurations. The average uncertainty values (calculated as the area between the uncertainty curve and the y-axis) for the uncooled and partially cooled cases are similar, with ±0.0374% for the uncooled case and ±0.0362% for the partially cooled case. For the fully cooled case, the average uncertainty is ±0.0678%. The maximum uncertainty in the uncooled and fully cooled vanes are similar, with respective values of ±0.197% and ±0.180%, while that of the partially cooled vane is much lower, at ±0.0692%.

Table 6-3: Average, Maximum Mass-Averaged Loss Uncertainty Values

Cooling configuration	Maximum Uncertainty in KE Loss Coefficient	Average Uncertainty in KE Loss Coefficient
Fully Cooled Vane	±0.180%	±0.0678%
Partially Cooled Vane	±0.0692%	±0.0362%
Uncooled Vane	±0.197%	±0.0374%

6.3 Uncertainty Analysis Limitations

Though the uncertainty analysis presented above takes many different variables and sources of error into account, there are several important limitations. First, the systematic uncertainty present in some experimental equipment is unknown. These unknown values include the systematic uncertainty in the inlet mass flow measurement, and the systematic uncertainties in the temperature, total pressure, and relative humidity factor measured at MF1. Also unknown is the systematic uncertainty caused by the radial traverse unit used to position the 5-hole probe, though the systematic uncertainty caused by the linear traverse unit is known.

Incorporating the systematic uncertainty of the inlet mass flow would increase the uncertainty in the mass flux ratio, which is used to calculate the kinetic energy loss coefficient. The rest of the missing systematic uncertainty values would have no effect on the kinetic energy loss coefficient before mass-averaging is performed, but instead would only impact the mass-averaged loss coefficient. Incorporating the systematic uncertainties present in the relative humidity factor, total pressure, and temperature values measured at MF1 would serve to increase the uncertainty in the density, as these values are used for calculating the gas constant, which is in turn used to calculate the density. Incorporating the uncertainty caused by the radial traverse unit would serve to increase the overall uncertainty in the area calculations, as the radial probe head position is used in these calculations.

The current uncertainty analysis also fails to include uncertainties that arise during the calibration process. As the calibration data is used for calculating the total and static pressure at the outlet, incorporating these uncertainties into the analysis would impact the uncertainty in the kinetic energy loss coefficient, both before and after mass-averaging.

Figure 6-9 displays the sensitivity of the uncertainty in the mass-averaged loss coefficient at each radial measurement point to increases in uncertainties of variables used for its calculation. For each of the variables tested, the uncertainty of the variable is increased by 1%, and the corresponding increase in the overall uncertainty is observed.

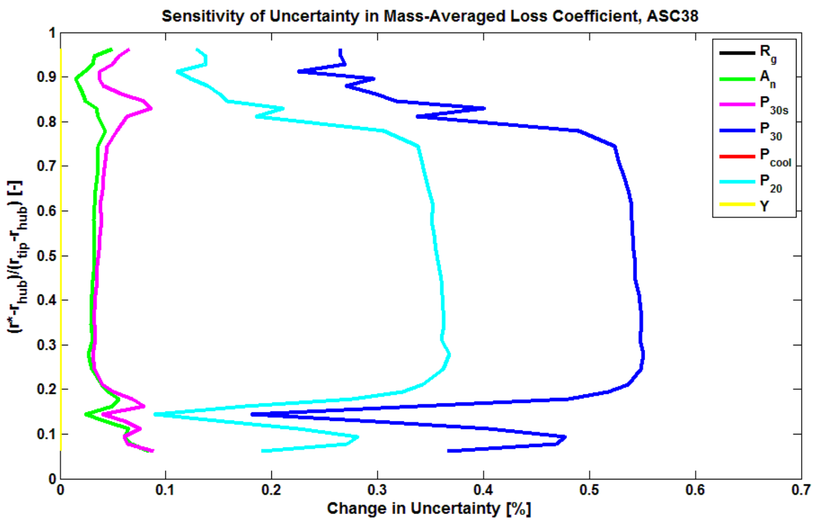

Figure 6-9: Sensitivity of Mass-Averaged Loss Uncertainty

Observing the figure above, it can be seen that increasing the uncertainty in the mass flux ratio *Y*, the gas constant R_g, or the pressure of the coolant air p_{cool} has no impact on the overall uncertainty in the mass-averaged loss coefficient. On the other hand, increasing the uncertainty in the total pressure at the outlet p_{30} or the total pressure at the inlet p_{20}

has a significant impact on the overall uncertainty. An increased uncertainty in the static pressure at the outlet p_{30s} or the area A_n also has a noticeable impact on the overall uncertainty in the mass-averaged loss coefficient, though smaller than the impact of increased uncertainty in p_{20} or p_{30}. This means that incorporating the systematic uncertainty in the radial traverse cart would have an impact on the overall uncertainty in the losses, while incorporating the other unknown systematic uncertainties would have no real impact. Incorporating the uncertainties due to the calibration process could also have a significant impact on the overall calculated uncertainty values.

The sensitivity of the mass-averaged loss coefficient to increases in its variables is greater than the sensitivity of the uncertainty in the mass-averaged loss coefficient to increases in its variables. Figure 6-10 displays the response of the mass-averaged loss coefficient to a 1% increase in the variables.

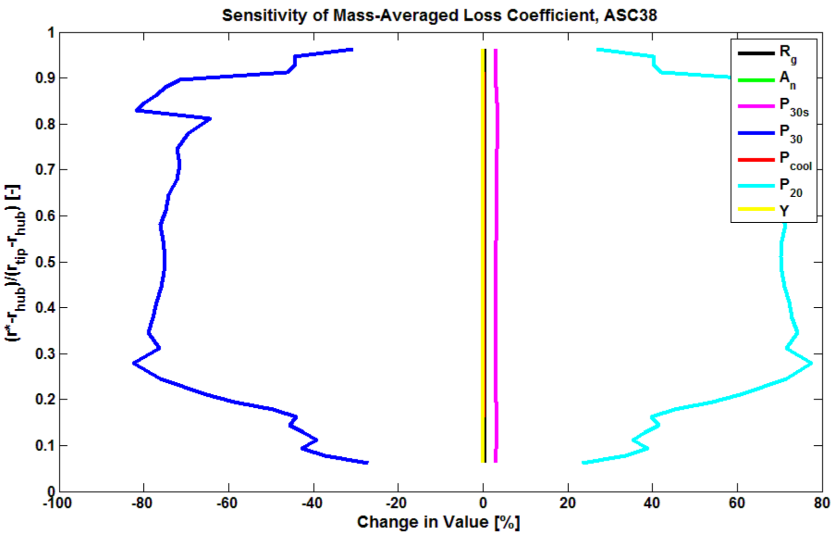

Figure 6-10: Sensitivity of Mass-Averaged Loss Coefficient

It can be observed that, analogous to the sensitivity of the mass-averaged loss coefficient uncertainty, the total pressure at the outlet p_{30} and the total pressure at the inlet p_{20} have the greatest impact on the mass-averaged loss coefficient value. The changes caused by increasing these values are large: a 1% increase in p_{30} causes up to an 80% decrease in the loss coefficient value, while a 1% increase in p_{20} causes up to an 80% increase in the loss coefficient value. A 1% increase in the static pressure at the outlet causes a moderate increase in the value of the mass-averaged loss coefficient, while increases in the area, mass flux ratio, coolant air pressure, and gas constant have almost no effect on the value of the mass-averaged loss coefficient.

6.3.1 Incorporating Uncertainty from the Calibration Process

Although the uncertainty in the calibration data has not been incorporated into the uncertainty calculations in this study, a method for calculating and incorporating these uncertainties into future work has been developed.

6.3.1.1 <u>Calibration of 5-hole probe</u>

Before detailing the method for calculating uncertainty in the calibration measurements, the calibration process must first be understood. The 5-hole probe must be calibrated for a range of different operating points before it can be used for investigating unknown flow fields. The current probe calibration was performed for Mach numbers from 0.1 to 0.95, pitch angles of $\beta = \pm 20^{\circ}$ and yaw angles of $\alpha = \pm 20^{\circ}$. In the probe calibration procedure, for different dimensionless coefficients are calculated for each operating point, which can then be used in determining the flow parameters of unknown flow fields.

Figure 6-11 shows the VM100 wind tunnel which is used for the probe calibration procedure. The air supply system is set up as described in section 4.1.1.

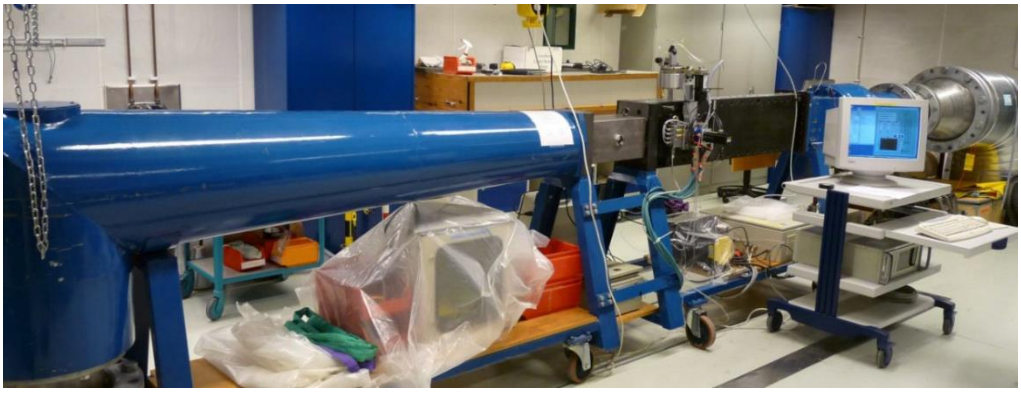

Figure 6-11: VM100 Wind Tunnel (Bartl 2010)

The 5-hole probe is attached to the traverse mechanism shown in Figure 6-12. This traverse mechanism sets the yaw and pitch angles to values between ±20˚, but keeps the tip of the probe head at exactly the same spot in the calibration zone.

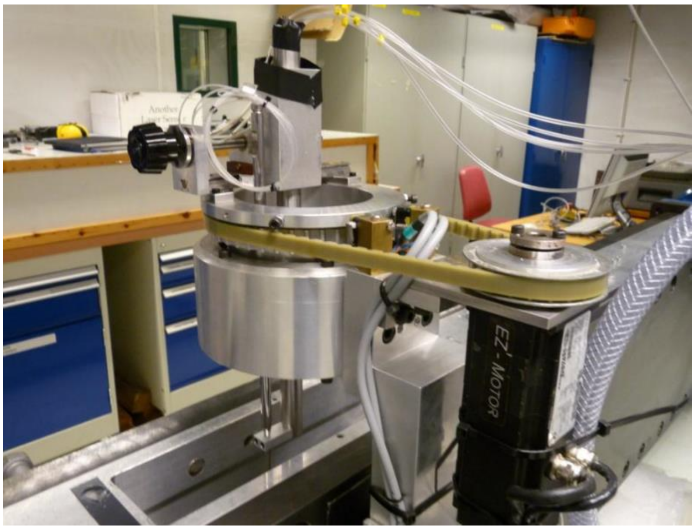

Figure 6-12: The calibration traverse mechanism (Bartl 2010)

The calibration test rig is kept at 30˚C, which is the same as the operating temperature in the ASC. The flow channel is designed in order to generate a well-defined and uniform flow in the calibration zone. The operating point is controlled by adjusting valves SV1, SV2, SV3, and SV4 in the air supply system.

During the calibration procedure, seven different pressures are measured. These pressures are the total pressure in the flow channel, the static pressure in the test section, and the five probe pressures. The five pressures measured in the probe are defined according to Figure 6-13.

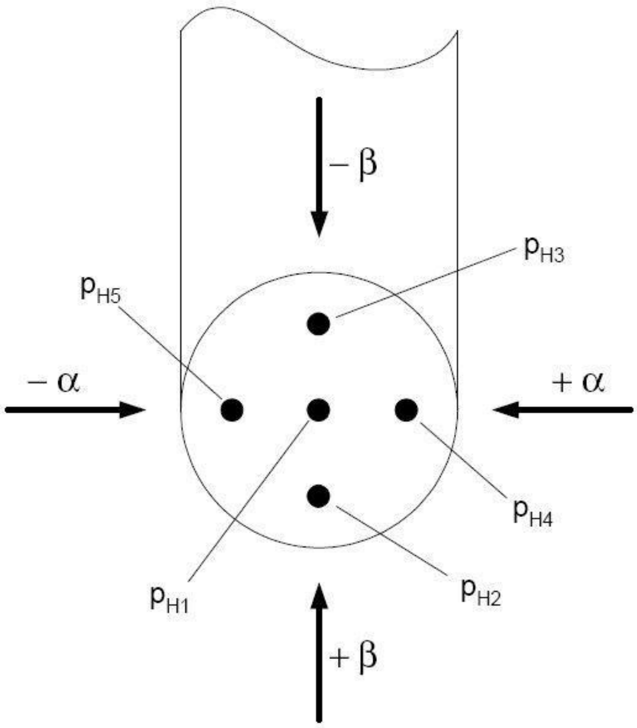

Figure 6-13: Pressures measured by the 5-hole probe

Once the data has been collected, the calibration coefficients can be calculated by:

Total pressure coefficient: $k_1 = \frac{p_0 - p_{H1}}{p_{H1} - p_{ave}}$

Static pressure coefficient: $k_2 = \frac{p_0 - p_s}{p_{H1} - p_{ave}}$

Yaw angle coefficient: $k_3 = \frac{p_{H4} - p_{H5}}{p_{H1} - p_{ave}}$

Pitch Angle Coefficient: $k_4 = \frac{p_{H2} - p_{H3}}{p_{H1} - p_{ave}}$

where $p_{ave} = \frac{p_{H2} + p_{H3} + p_{H4} + p_{H5}}{4}$

All variables mentioned in these equations represent values collected during the calibration process, rather than during the experimental trials. A Matlab function has been written which uses these pre-calculated calibration coefficients to determine the total pressure, static pressure, pitch angle, and yaw angle distributions in unknown flow fields.

6.3.1.2 Total Pressure, Static Pressure Coefficient Uncertainty

As seen in Section 6.1, the calibration coefficients k_1 and k_2 calculated during the calibration process are used to calculate the total pressure and static pressure at the outlet for the measurement data. In order to incorporate the uncertainty from the calibration process into these values, the uncertainty in calibration coefficients k_1 and k_2 must be calculated.

The uncertainty in k_1 can be calculated by:

$$wk_1 = \sqrt{\left(\frac{\partial k_1}{\partial p_0} wp_0\right)^2 + \left(\frac{\partial k_1}{\partial p_{H1}} wp_{H1}\right)^2 + \left(\frac{\partial k_1}{\partial p_{ave}} wp_{ave}\right)^2}$$

where

$$\frac{\partial k_1}{\partial p_0} = \frac{1}{p_{H1} - p_{ave}}$$

$$\frac{\partial k_1}{\partial p_{H1}} = \frac{p_{ave} - p_0}{(p_{H1} - p_{ave})^2}$$

$$\frac{\partial k_1}{\partial p_{ave}} = \frac{p_0 - p_{H1}}{(p_{H1} - p_{ave})^2}$$

and

$$wp_{ave} = \sqrt{(\frac{1}{4} wp_{H2})^2 + (\frac{1}{4} wp_{H3})^2 + (\frac{1}{4} wp_{H4})^2 + (\frac{1}{4} wp_{H5})^2}$$

The experimental equipment used to measure the pressures is the same as for the test rig, so the systematic and random uncertainties of these pressure variables can be determined in the same way as described for the test rig in Section 6.1.

The uncertainty in k_2 can be calculated by:

$$wk_2 = \sqrt{\left(\frac{\partial k_1}{\partial p_0} wp_0\right)^2 + \left(\frac{\partial k_1}{\partial p_s} wp_s\right)^2 + \left(\frac{\partial k_1}{\partial p_{H1}} wp_{H1}\right)^2 + \left(\frac{\partial k_1}{\partial p_{ave}} wp_{ave}\right)^2}$$

where

$$\frac{\partial k_2}{\partial p_0} = \frac{1}{p_{H1} - p_{ave}}$$

$$\frac{\partial k_2}{\partial p_s} = \frac{-1}{p_{H1} - p_{ave}}$$

$$\frac{\partial k_2}{\partial p_{H1}} = \frac{-(p_0 - p_s)}{(p_{H1} - p_{ave})^2}$$

and

$$\frac{\partial k_2}{\partial p_{ave}} = \frac{p_0 - p_s}{(p_{H1} - p_{ave})^2}$$

Once the uncertainties in the total pressure and static pressure coefficients have been calculated, the method used to calculate the uncertainty in total pressure and static pressure in the test rig must be updated. Recall that the total pressure at the outlet in the annular sector cascade was calculated as:

$$p_{30} = k_1(p_1 - p_{ave}) + p_1$$

The uncertainty in outlet total pressure should now be calculated by:

$$wp_{30} = \sqrt{\left(\frac{\partial p_{30}}{\partial k_1} wk_1\right)^2 + \left(\frac{\partial p_{30}}{\partial p_1} wp_1\right)^2 + \left(\frac{\partial p_{30}}{\partial p_{ave}} wp_{ave}\right)^2}$$

where

$$\frac{\partial p_{30}}{\partial k_1} = p_1 - p_{ave}$$

The other differentials in this equation are calculated as described in Section 6.3.

As described in Section 6.1, the static pressure at the outlet in the annular sector cascade was calculated as:

$$p_{30s} = p_{30} - k_2(p_1 - p_{ave})$$

The uncertainty in outlet total pressure should now be calculated by:

$$wp_{30s} = \sqrt{\left(\frac{\partial p_{30s}}{\partial k_2} wk_2\right)^2 + \left(\frac{\partial p_{30s}}{\partial p_{30}} wp_{30s}\right)^2 + \left(\frac{\partial p_{30s}}{\partial p_1} wp_1\right)^2 + \left(\frac{\partial p_{30s}}{\partial p_{ave}} wp_{ave}\right)^2}$$

where

$$\frac{\partial p_{30s}}{\partial k_2} = p_1 - p_{ave}$$

The other differentials in this equation are calculated as described in Section 6.3. The yaw and pitch angle coefficients are not used in any of the calculations, and so it is not necessary to calculate the uncertainties in these coefficients.

7 CONCLUSIONS

Improvements made to the area cell calculation method have improved the overall accuracy of the results. These changes had the greatest impact on the mass-averaged kinetic energy loss coefficient, where a reduction in value of up to 1.3% could be observed. Results from the uncertainty analysis showed that uncertainty in the kinetic energy loss coefficient is highest in the wake region, as well as regions near the hub and tip. These are the regions subjected to secondary flow and boundary layer effects, where there are large local deviations from the mainstream flow properties.

One major finding from the uncertainty analysis is that both the mass-averaged loss coefficient values and their associated uncertainties were found to be lower in the uncooled and partially cooled cases than in the fully cooled case, and the partially cooled vane experienced a smaller increase in uncertainty close to the tip than did the uncooled and fully cooled vanes. This indicates that partial film cooling of vanes can have a beneficial effect in terms of reducing aerodynamic losses, as well as the uncertainties associated with calculating such values.

A second major finding from the uncertainty analysis is a strong correlation between areas of high vorticity and areas of high uncertainty. Regions with especially high uncertainty could often be connected to places where positive and negative vorticities met, indicating that measurement uncertainties are very high in areas with volatile flow conditions. For all cooling cases, vorticity was found to be highest in the hub, tip, and wake regions. Overall, vorticities were found to be higher for the fully cooled vane than for the partially cooled and uncooled vanes, and more areas outside the hub, tip, and wake regions were subject to vorticity than in the other cooling configurations.

7.1 Future Work

One important task for future work is eliminating some of the limitations in the uncertainty analysis discussed in Section 6.3. This includes determining the missing systematic uncertainty values, and incorporating the uncertainties from the calibration process into the overall uncertainty measurement. A method for determining the uncertainties in the calibration data was presented in Section 6.3.1, but has not yet been applied to the calibration data.

A second task for future work is calculating and analyzing the circumferential and radial components of the vorticity. A method for calculating these vorticity components has been presented in Section 5.4.2, but has not been applied to any experimental data.

8 REFERENCES

Bartl, J. (2010). *Loss Measurements and Endwall Flow Investigations on an Annular Sector Cascade*. Royal Institute of Technology, Department of Energy Technology. Stockholm: EKV.

Bronkhorst High-Tech B.V. (no date). *EL-FLOW ® Metal Sealed Gas Mass Flow Meters/Controllers*. Retrieved from Bronkhorst High Tech: www.bronkhorst.com.

El-Gabry, L. *et. al.* (2012). *Measurements of Hub Flow Interaction on Film Cooled Nozzle Guide Vanes in Transonic Annular Cascade*. Proceedings of ASME Turbo Expo 2012. Copenhagen, Denmark.

Fridh, J. (2012). *Experimental Investigation of Performance, Flow Interactions, and Rotor Forcing in Axial Partial Admission Turbines.* Royal Institute of Technology, Department of Energy Technology. Stockholm: EKV.

Glodic, N. (2008). *Experimental Analysis of Aerodynamic Losses of a Film Cooled Nozzle Guide Vane in an Annular Sector Cascade*. Royal Institute of Technology, Department of Energy Technology. Stockholm: EKV.

Gregory-Smith, D.G., Graves, C.P., and Walsh, J.A. (1988, January). Growth of Secondary Losses and Vorticity in an Axial Turbine Cascade. *Journal of Turbomachinery*, 110, pages 1-8.

Kline, S. and McClintock, F. (1953, January). Describing Uncertainties in Single-Sample Experiments. *Mechanical Engineering*, 3.

Langston, L.S., Hooper, R.M., and Nice, M.L. (1977). Three-Dimensional Flow Within a Turbine Cascade Passage. *Journal of Engineering for Power*, 99 (1), pages 21-28.

Pico Technology (no date). *PT100 Platinum Resistance Thermometers*. Retrieved from Pico Technology: www.picotech.com.

Pütz, F.M. (2010). *Load, Secondary Flow and Turbulence Measurements on Film Cooled Nozzle Guide Vanes in a Transonic Annular Sector Cascade*. Royal Institute of Technology, Department of Energy Technology. Stockholm: EKV.

Roach, P. (1987). The Generation of Nearly Isotropic Turbulence by Means of Grids. *International Journal of Heat and Fluid Flow*, 8 (2).

Saha, R. *et. al.* (2012). *Experimental Studies of Leading Edge Contouring Influence on Secondary Losses in Transonic Annular Cascade*. Proceedings of ASME Turbo Expo 2012. Copenhagen, Denmark.

Saha, R. *et. al.* (2013). *Suction Side and Pressure Side Film Cooling on Vane Aero Performance in a Transonic Annular Cascade*. Proceedings of ASME Turbo Expo 2013. San Antonio, Texas.

Sudharsan, H. (2012). *Experimental Uncertainty Study in an Annular Sector Cascade for Film Cooled Nozzle Guide Vane*. Royal Institute of Technology, Department of Energy Technology. Stockholm: EKV.